International Journal of Hydrogen Energy 79 (2024) 883–900

Contents lists available at ScienceDirect

International Journal of Hydrogen Energy

journal homepage: www.elsevier.com/locate/he

Phenomenal study of microbial impact on hydrogen storage in aquifers: A coupled multiphysics modelling

Qi Gao [a,*], Jishan Liu [a], Derek Elsworth [b]

[a] School of Engineering, The University of Western Australia, Perth, WA 6009, Australia
[b] Department of Energy and Mineral Engineering, G3 Centre and Energy Institute, The Pennsylvania State University, University Park, PA, 16802, USA

ARTICLE INFO

Keywords:
Underground hydrogen storage
Microbial clogging
Hydrogen consumption
Mineral dissolution/precipitation

ABSTRACT

Underground hydrogen storage (UHS) has been considered as an integral part of energy transition from fossil fuels to renewable sources. Porous aquifers can serve as typical sites for this purpose due to their worldwide distribution and huge storage capacity. However, the diverse microbial species that inhabit the aquifers are known to be able to catalyze in-situ biochemical reactions within the hosting rock. These reactions can normally lead to microbial consumption of hydrogen, microbial clogging of pore space and thus affect hydrogen injection and withdrawal rates as reported in the literature. So far, these phenomena have been widely reported but rarely quantified. In this study, we build a coupled hydrological-mechanical-chemical-biological (HMCB) multiphysics model to simulate these microbe-related processes during UHS in aquifers. The model consists of a complete set of partial differential equations to describe: (1) rock deformation; (2) water-hydrogen two-phase flow; (3) microbes and dissolved hydrogen transport; (4) mineral dissolution/precipitation; and (5) microbial activities involving adsorption/desorption and growth/decay. All these processes are linked together through the porosity/permeability models which consider the joint impacts of microbial clogging, mineral dissolution/precipitation and effective stress. This multiphysics model is verified against laboratory biochemical reaction data and microbial transport data. Then, the verified model is used to investigate the impacts of iron-reduction bacteria (IRB) activities on UHS in aquifers. Based on the simulation results, it can be concluded that (1) hydrogen saturation at the top surface of the aquifer is the greatest while microbial activities surrounding the injection well is stimulated the most; (2) microbial activities influence the initial few cycles of hydrogen injection and withdrawal but the impacts gradually diminish with the dissolution of Fe_2O_3; (3) hydrogen recovery efficiency is degraded due to the combined effects of hydrogen consumption, water production and microbial clogging with the microbial clogging impact being the most significant; and (4) effective stress impacts aquifer permeability throughout UHS operations while microbial clogging influences it in the initial few cycles. For mineral dissolution/precipitation, the impact can be neglected.

1. Introduction

In the context of decarbonization and achieving the net-zero emission target, renewable energies like solar energy, wind energy and tidal energy are now attracting more and more attention around the world [1–4]. However, production of these renewable energies is greatly dependent on seasonal atmospheric conditions (i.e., sunlight level and wind scale) and geographic locations [5]. Considering the annual varying but steady energy demand, the fluctuating production of these renewable energies inevitably leads to the mismatches between energy demand and supply [6]. Therefore, renewable energy production with excess energy storage should be adopted to bridge this energy gap [7].

The excess renewable energy can be converted to hydrogen, a type of low-carbon energy carrier, and then stored to be used during high energy demand periods. As surface hydrogen storage facilities have limited storage and discharge capacity, UHS in geo-structures like salt caverns, aquifers and depleted oil and gas reservoirs is required [8–12]. Compared to surface storage options, UHS requires lower investment and smaller surface space, offers higher safety standards, induces less environmental impacts, and more importantly provides a large-scale and long-term storage option [13–17]. However, most of these subsurface environments are not life-free and harbor a variety of microbial

* Corresponding author.
E-mail address: qi.gao@research.uwa.edu.au (Q. Gao).

https://doi.org/10.1016/j.ijhydene.2024.07.004
Received 22 April 2024; Received in revised form 8 June 2024; Accepted 1 July 2024

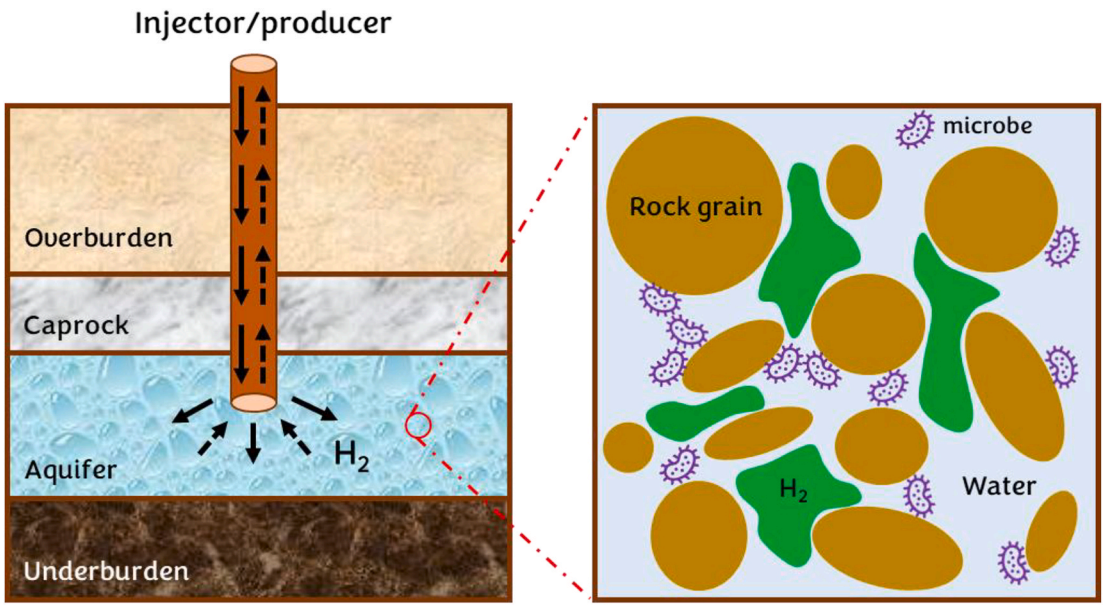

Fig. 1. Schematic diagram of hydrogen injection and withdrawal in aquifers where microbes live.

communities [18–21]. The activities of these microbes can be stimulated by the stored hydrogen and then have significant impacts on UHS operations.

In some underground gas storage (UGS) field tests, the phenomenon of microbial consumption of hydrogen has been observed. For example, an UGS project in Lobodice, Czech Republic [22] reported that nearly half of the stored hydrogen in sandstone reservoir was microbially converted into hydrogen sulfide and methane. Isotropic analysis has proofed the microbial origin of the formed gas. Meanwhile, a decrease in reservoir pressure and an increase in microbe cell numbers during UGS operations were reported. In another example of UGS project in Lehen, Austria [23,24], 10% hydrogen was mixed with natural gas and then stored in sandstone reservoir for four months. In this period, nearly 16% of the stored hydrogen cannot be recovered. The DNA analysis and RNA data suggest that different microbial metabolisms like methanogenesis, acetogenesis and sulfate-reduction could be triggered in this process. In addition, the Argentinian HyChico project [25] stored hydrogen in a depleted sandstone reservoir. During the storage cycle, microbe-induced hydrogen loss was also observed.

In addition to field tests, laboratory experiments have also been conducted to investigate the impacts of microbial activities on UHS. Strobel et al. [26] and Khajooie et al. [27] performed a series of biochemical experiments by use of methanogens and hydrogen/carbon dioxide gas mixture. The experiments were performed in pressurized batch reactors and the experimental results showed that microbial metabolism and growth leads to the decrease of hydrogen concentration and increase of methane concentration. Liu et al. [28] conducted the pore-scale biochemical experiments by use of halophilic sulfate-reducing bacteria and hydrogen. In their experiments, a silicon-wafer micromodel with a pore pattern from natural sandstone was used for direct observation of microbe-induced sulfate reduction under the conditions of 35 bar and 37 °C. A significant loss of hydrogen from microbial consumption and a change in surface wettability due to microbial growth were observed from the experiments.

Although laboratory experiments are the most direct way to study microbial impacts on UHS, it is sometimes expensive, time-consuming and massive manpower required. Even in some cases, the experiments can only be performed under the very simple conditions. Therefore, theoretical approaches are vital for us to study this problem. Strobel et al. [26] proposed a mathematical model for microbial growth, substrates conversion and phase mass transfer in batch reactors. This model can only be used to quantify the microbial impacts under the static conditions while for UHS in porous reservoirs where fluid flow involves the model cannot be applied. Ebigbo et al. [29] proposed a numerical model to investigate microbial impacts on UHS which couples biofilm growth process with fluid flow and solute transport processes, but the model application is limited to the pore scale. To this end, Hagemann et al. [30] developed a two-phase bio-reactive transport model to study microbial impacts on UHS in porous reservoir. In their model, microbial growth/decay was considered. Applying this model, the variation of gas composition and concentration during UHS can be captured but an important mechanism, i.e., microbial clogging of pore space, was missed in their study. Eddaoui et al. [31] built a multi-component two-phase flow model to study the impact of microbial clogging on UHS in porous reservoir. In their model, both microbial growth/decay and adsorption/desorption were considered. However, the model only studied microbial impacts on porosity/permeability variation during UHS while many other important parameters like gas composition, hydrogen injection and withdrawal rates, and hydrogen recovery factor were not investigated.

As can be summarized from the above literature review, both field tests and laboratory experiments have confirmed the undesired side effects induced by microbial activities during UHS. To quantify these microbial impacts, several theoretical studies have been undertaken. However, works on modeling the impacts of microbial activities on UHS in porous reservoirs are still very limited at the current stage which limits our understanding of this problem. To this end, a coupled HMCB multiphysics model is developed in this work to quantify all important processes involved. In the following, the conceptual model for UHS in aquifers in first introduced. In this conceptual model, the impacts of microbial activities on UHS are illustrated in detail. Then, a complete set of partial differential equations are defined to describe the involved processes with all these processes linked by the porosity and permeability models. After that, the proposed model is verified against laboratory iron reduction data and microbial transport data. In the end, the multiphysics model is applied to analyze microbial impacts on UHS in aquifers.

2. The conceptual model

The starting point to model the impacts of microbial activities on UHS in aquifers is to understand the fundamental processes involved.

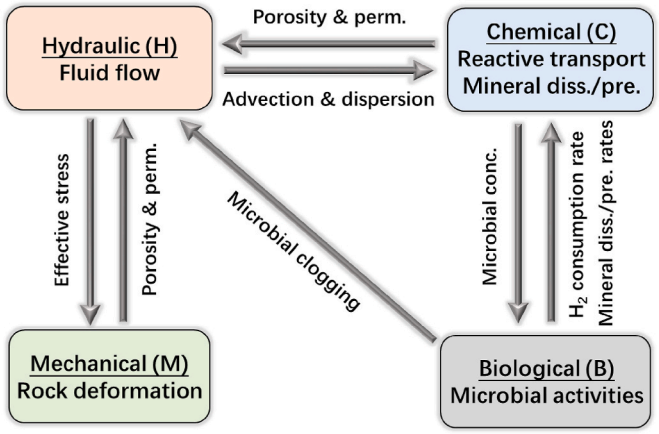

Fig. 2. Coupling relations among different physical fields during UHS in aquifers.

Table 1
Input parameters for model verification on the chemical reaction process.

Parameters (unit)	Symbols	Values
The maximum microbial growth rate (1/h)	$g_{1\ max}$	0.08
Microbial decay rate (1/h)	d_1	0.005
Reaction yield coefficient (mol/m^3/h)	$1/Y$	0.02
Half-saturation constant for iron reduction (mg/mL)	$K_{m/s}$	0.2
Half-saturation constant for microbial growth (mg/mL)	$K_{H_2/s}$	0.5
Half-saturation constant for microbial growth (mg/mL)	$K_{Fe(III)/s}$	200
Initial hydrogen concentration in aqueous phase (mg/mL)	$C_{H_2,0}$	8.5e-10
Initial microbial concentration in aqueous phase (mg/mL)	$C_{m,0}$	1e-4
Initial Fe(III) concentration (mol/m^3)	$C_{Fe(III),0}$	500
Initial Fe(II) concentration (mol/m^3)	$C_{Fe(II),0}$	0

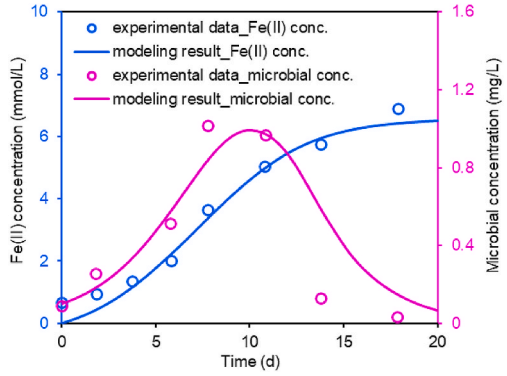

Fig. 3. Comparison between the modeling results and the experimental data reported by Roden and Zachara [45].

During UHS, hydrogen is cyclically injected into and withdrawn from the subsurface aquifers, see Fig. 1. Depending on the underground pressure, temperature and salinity conditions, a certain amount of hydrogen would dissolve into the formation water. The dissolved hydrogen serves as one of the most important electron donors for many subsurface microbial processes. According to the available literatures, it is expected that at least seven hydrogenotrophic microbial processes could be important for UHS [32,33]. Simultaneous survival and competition among these microbes are possible. Studies have also shown that these microbes have different minimum threshold concentrations for hydrogen consumption. Among these microbes, IRB have the lowest threshold concentration and consequently have the best potential to out-compete other species [30]. Therefore, in this work, we take IRB as an example to investigate the impacts of microbial activities on UHS

Table 2
Input parameters for model verification on the microbial transport process.

Parameters (unit)	Symbols	Values
Reversible microbial adsorption rate (1/h)	k_1	0.065
Microbial desorption rate (1/h)	k_2	0.0012
Irreversible microbial adsorption rate (1/h)	k_3	0.01
Microbial growth rate (1/h)	g_1	2.5e-3/5e-3/1e-2
Microbial decay rate (1/h)	d_1	0
Microbial density (kg/m^3)	ρ_m	1600

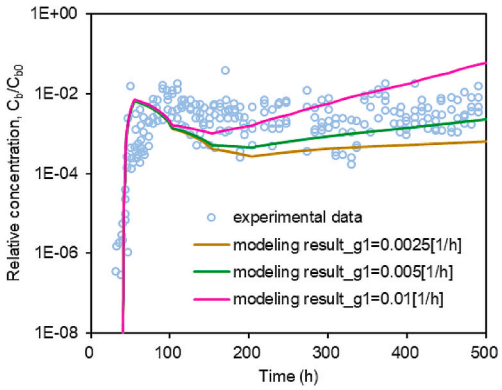

Fig. 4. Comparison between the modeling results and the experimental data reported by Henry et al. [46].

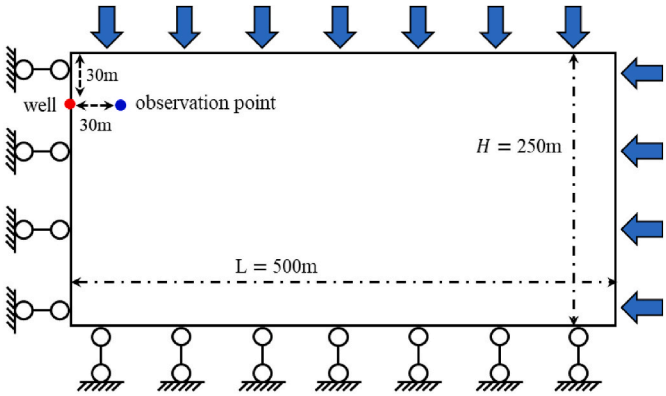

Fig. 5. Geometry of the 2D numerical model for UHS modeling.

in aquifers. It is worth noting that microbes can only survive in subsurface formations under constrained temperature and salinity conditions [34] and in this work we assume that the aquifer we investigate satisfy these conditions.

Following hydrogen injection, the elevation of hydrogen concentration in formation water stimulates the growth of IRB in subsurface pore space. The microbial growth occupies a fraction of pore space and reduces the porosity and permeability of aquifers. Thus, bioclogging occurs during UHS and this will impact hydrogen injection and withdrawal rates. Meanwhile, during IRB growth, specific enzymes are produced which can catalyze the chemical reaction between hydrogen and the mineral Fe_2O_3 [32] in porous rock:

$$3Fe_2O_3 + H_2 \rightarrow 2Fe_3O_4 + H_2O \quad (1)$$

The above reaction couples hydrogen oxidation with Fe(III) reduction. From the chemical reaction equation, it can be known that during iron reduction process a certain amount of hydrogen is consumed and additionally a certain amount of water is produced. This process lowers hydrogen saturation and relative permeability in aquifers and thus

Table 3
Input parameters for the base case simulation.

Parameters (unit)	Symbols	Values	References
Pore compressibility (MPa^{-1})	c_p	0.02	–
Elastic modulus (GPa)	E	20	–
Poisson's ratio	ν	0.2	–
Confining pressure (MPa)	σ_c	20	–
Initial porosity	$\varnothing_0$	0.1	–
Initial permeability (m^2)	k_0	1e-13	–
Rock density (kg/m^3)	ρ_c	2400	–
Reversible microbial adsorption rate (1/h)	k_1	0.065	Kim [53]; Li et al. [39]
Microbial desorption rate (1/h)	k_2	0.0012	Kim [53]; Li et al. [39]
Irreversible microbial adsorption rate (1/h)	k_3	0.01	Kim [53]; Li et al. [39]
The maximum microbial growth rate (1/h)	$g_{1\ max}$	0.024	Kim [53]; Li et al. [39]
Microbial decay rate (1/h)	d_1	0.005	Kim [53]; Li et al. [39]
Microbial density (kg/m^3)	ρ_m	1600	Kim [53]; Li et al. [39]
Reaction yield coefficient ($mol/m^3/h$)	$1/Y$	0.02	–
Half-saturation constant for iron reduction (mg/mL)	$K_{m/s}$	0.2	–
Half-saturation constant for microbial growth (mg/mL)	$K_{H_2/s}$	0.5	–
Half-saturation constant for microbial growth (mg/mL)	$K_{Fe_2O_3/s}$	200	–
Hydrodynamic dispersion coefficient for hydrogen (m^2/s)	D_{H_2}	1e-6	–
Hydrodynamic dispersion coefficient for microbe (m^2/s)	D_m	1e-9	Kim [53]; Li et al. [39]
Initial water saturation	$S_{w,0}$	1	Zhao et al. [54]
Irreducible water saturation	S_{wi}	0.2	Zhao et al. [54]
Residual gas saturation	S_{gr}	0	Zhao et al. [54]
Nonwetting phase entry pressure (KPa)	p_e	5	Zhao et al. [54]
Pore size distribution coefficient	λ	2	–
Initial hydrogen concentration in aqueous phase (mg/mL)	$C_{H_2,0}$	0	–
Initial microbial concentration in aqueous phase (mg/mL)	$C_{m,0}$	0.0001	–
Initial fraction of porosity occupied by reversibly adsorbed microbes	$\varnothing_{1,0}$	1e-6	–
Initial fraction of porosity occupied by irreversibly adsorbed microbes	$\varnothing_{2,0}$	1e-6	–
Initial Fe_2O_3 concentration in porous rock (mol/m^3)	$C_{Fe_2O_3,0}$	450	–
Initial Fe_3O_4 concentration in porous rock (mol/m^3)	$C_{Fe_3O_4,0}$	0	–

impacts hydrogen injection and withdrawal rates as well. From the chemical reaction equation, it can also be known that mineral dissolution and precipitation simultaneously take place during UHS. The dissolution of Fe_2O_3 leads to porosity and permeability increase while the precipitation of Fe_3O_4 leads to porosity and permeability decline. Thus, hydrogen injection and withdrawal rates may also be changed under the impacts of these two competing processes.

Overall, UHS in aquifers involves the interactions of multiple processes. These processes mainly include rock deformation, water-gas two-phase flow, multispecies reactive transport, and microbial growth/decay and adsorption/desorption. All these processes can be linked together through the porosity and permeability models. During UHS in aquifers, rock porosity and permeability are mainly influenced by the following three factors including effective stress, microbial clogging, and mineral dissolution and precipitation.

3. Governing equations for the coupled processes

From the above introduced conceptual model, it can be known that complex interactions occur among rock, formation water, hydrogen and microbes during UHS in aquifers. These interactions exert strong influences on rock deformation, water-gas two-phase flow, multispecies reactive transport, microbial activities, and porosity and permeability change. Therefore, in this work, we define UHS operations as the coupled HMCB processes, which implies that one physical process affects the initiation and progress of another. The inclusion of cross-coupling relations among these physical processes is the key to formulate the mathematical model to describe UHS operations. In the following, the derivation of the governing equations for the coupled processes involved is presented.

3.1. Rock deformation

In the following equations, all derivations are made after the traditional conventions: A comma followed by subscripts represents the differentiation with respect to spatial coordinates, and repeated indices in the same equation imply the summation over the range of indices. Following the conventions, the stress equilibrium equation ignoring the inertial term is expressed as:

$$\sigma_{ij,j} + f_i = 0 \tag{2}$$

where σ_{ij} is the component of stress tensor, and f_i is the component of body force.

The relation between strain and displacement is expressed as:

$$\varepsilon_{ij} = \frac{1}{2}\left(u_{i,j} + u_{j,i}\right) \tag{3}$$

where ε_{ij} is the component of strain tensor, and u_i is the component of displacement.

The relation between strain and stress can be defined in the form of:

$$\varepsilon_{ij} = \frac{1}{2G}\sigma_{ij} - \left(\frac{1}{6G} - \frac{1}{9K}\right)\sigma_{kk}\delta_{ij} + \frac{\alpha}{3K}p\delta_{ij} \tag{4}$$

where G is shear modulus, K is bulk modulus, α is Biot coefficient, $\sigma_{kk} = \sigma_{11} + \sigma_{22} + \sigma_{33}$, δ_{ij} is Kronecker delta, and p is pore pressure.

Integrating Eqs. (2)–(4), the Navier-type equation for rock deformation can be derived:

$$Gu_{i,kk} + \frac{G}{1-2\nu}u_{k,ki} - \alpha p_{,i} + f_i = 0 \tag{5}$$

It should be mentioned that water-gas two-phase flow presents in aquifers during UHS. Thus, the pore pressure term in Eq. (5) should be treated as the average pressure of water and gas phases [35,36]:

$$p = S_w p_w + S_g p_g \tag{6}$$

where S_w and S_g represent the water saturation and hydrogen saturation, respectively. p_w and p_g represent the water pressure and hydrogen pressure, respectively.

3.2. Water-gas two-phase flow

During UHS in aquifers, water-gas two-phase flow presents in the pore system. The mass conservation equation for each phase can be expressed as:

$$\frac{\partial(\varnothing S_w \rho_w)}{\partial t} = \nabla \bullet \left[\rho_w \frac{k k_{rw}}{\mu_w}(\nabla p_w - \rho_w g h)\right] + Q_w \tag{7}$$

$$\frac{\partial(\varnothing S_g \rho_g)}{\partial t} = \nabla \bullet \left[\rho_g \frac{k k_{rg}}{\mu_g}\left(\nabla p_g - \rho_g g h\right)\right] + Q_g \tag{8}$$

where $\varnothing$ is porosity; ρ_w and ρ_g are densities of water and hydrogen, respectively; k is absolute permeability; k_{rw} and k_{rg} are relative permeabilities of water and hydrogen, respectively; μ_w and μ_g are viscosities of water and hydrogen, respectively; g is gravitational acceleration; Q_w and Q_g are source terms for water and hydrogen, respectively, which are

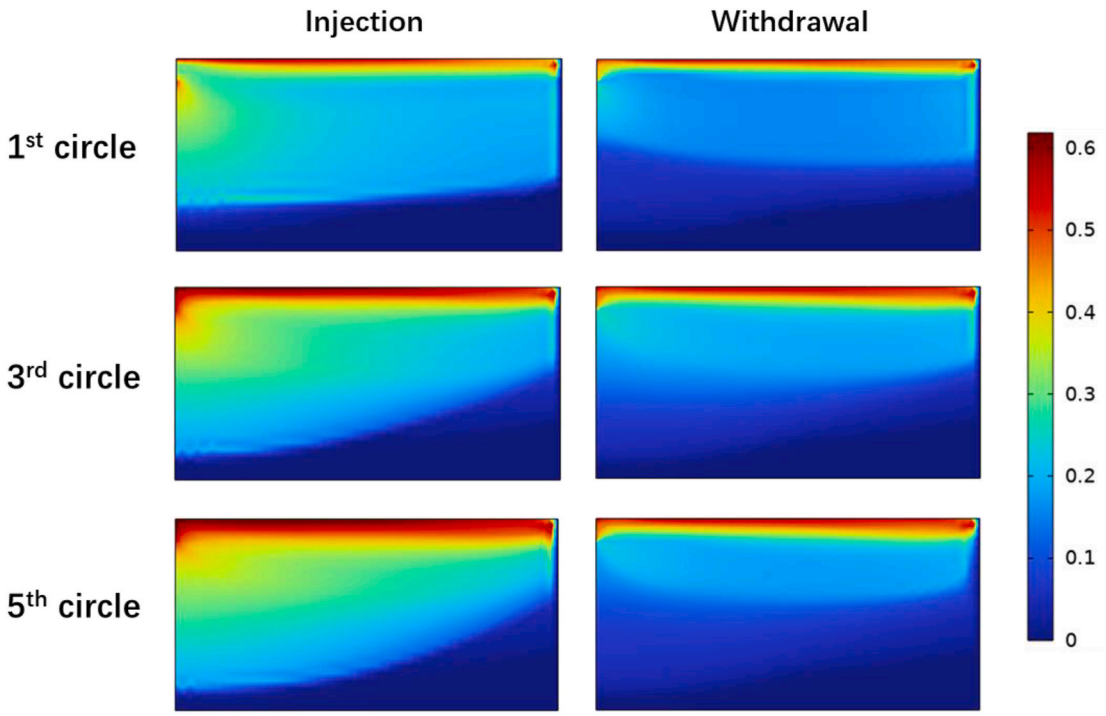

Fig. 6. Hydrogen saturation distribution in aquifer at the end of different injection and withdrawal cycles.

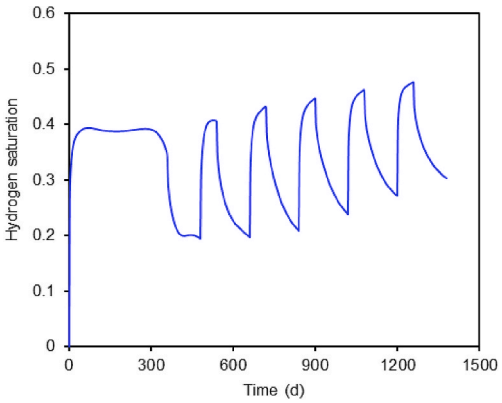

Fig. 7. Variation of hydrogen saturation at the observation point during cyclic hydrogen injection and withdrawal.

defined in the following forms:

$$Q_w = \frac{1}{Y} \bullet \frac{C_m}{K_{m/s} + C_m} \bullet M_{H_2O} \tag{9}$$

$$Q_g = -\xi\left(p_g - H_c C_{H_2}\right) \tag{10}$$

where $\frac{1}{Y}$ is the reaction yield coefficient; C_m is microbial concentration in aqueous phase; $K_{m/s}$ is the half saturation constant for iron reduction; M_{H_2O} is the molar mass of water; ξ is the hydrogen mass transfer rate from gaseous phase to aqueous phase; H_c is the corrected Henry's constant; and C_{H_2} is hydrogen concentration in aqueous phase.

Eqs. (7)–(10) define the fluids flow process during UHS in aquifers. In these equations, hydrogen density, viscosity and solubility are not constant and will change under different temperature, pressure and salinity conditions. The equations describing the variation of these hydrogen properties are provided in the appendixes at the end of the paper.

In addition, the total saturation of water and hydrogen should equal to one in the pore system:

$$S_w + S_g = 1 \tag{11}$$

In the pore system, water and hydrogen are separated by a well-defined interface and there exists a pressure difference between the two phases across the interface [37]. This pressure difference is called capillary pressure. The magnitude of capillary pressure is equivalent to the difference between the non-wetting phase pressure and wetting phase pressure. In this work, hydrogen is considered as the non-wetting phase and water is considered as the wetting phase. Thus, capillary pressure can be expressed as:

$$p_c = p_g - p_w \tag{12}$$

where p_c denotes the capillary pressure which can also be defined as a function of wetting phase saturation [38]:

$$p_c = p_e S_w^{*\,-1/\lambda} \tag{13}$$

where p_e is the entry pressure, S_w^* is the effective saturation of water, and λ is the pore size distribution coefficient.

The effective water saturation S_w^* and effective hydrogen saturation S_g^* are expressed in the forms of:

$$S_w^* = \frac{S_w - S_{wi}}{1 - S_{gr} - S_{wi}} \tag{14}$$

$$S_g^* = \frac{S_g - S_{gr}}{1 - S_{gr} - S_{wi}} \tag{15}$$

where S_{wi} is the irreducible water saturation, and S_{gr} is the residual hydrogen saturation.

Then, relative permeabilities of water and hydrogen can be defined as [38]:

$$k_{rw} = S_w^{*\,(3+2/\lambda)} \tag{16}$$

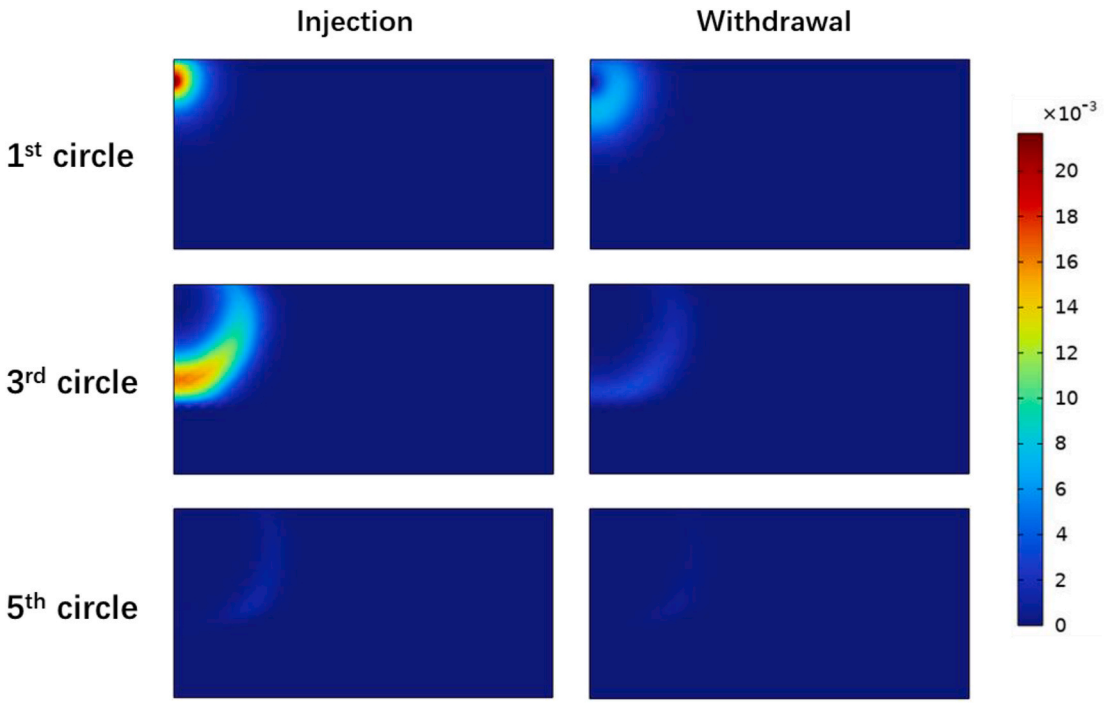

Fig. 8. Distribution of adsorbed microbe population ($\varnothing_1 + \varnothing_2$) in aquifer at the end of different injection and withdrawal cycles.

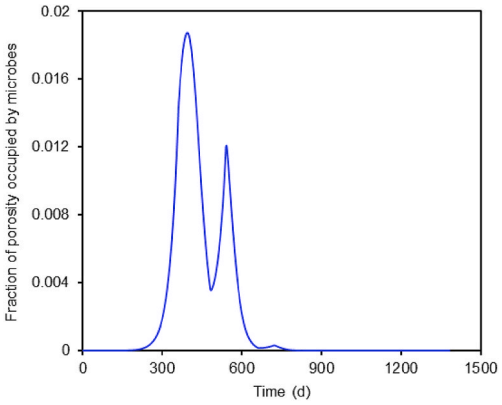

Fig. 9. Variation of adsorbed microbe population ($\varnothing_1 + \varnothing_2$) at the observation point during cyclic hydrogen injection and withdrawal.

$$k_{rg} = S_g^{*2}\left[1 - \left(1 - S_g^{*}\right)^{(1+2/\lambda)}\right] \tag{17}$$

3.3. Multispecies reactive transport

During UHS in aquifers, the movement of dissolved hydrogen and microbes in aqueous phase is mainly controlled by advective-dispersive transport [39,40]. The transport equations for dissolved hydrogen and microbes can be expressed as follows:

$$\frac{\partial(\varnothing S_w C_{H_2})}{\partial t} = \nabla \bullet (\varnothing S_w D_{H_2} \nabla C_{H_2}) - \nabla \bullet (v_w C_{H_2}) + R_{H_2} \tag{18}$$

$$\frac{\partial(\varnothing S_w C_m)}{\partial t} = \nabla \bullet (\varnothing S_w D_m \nabla C_m) - \nabla \bullet (v_w C_m) + R_m \tag{19}$$

where C_{H_2} and C_m represent hydrogen concentration and microbial concentration in the aqueous phase, respectively; D_{H_2} and D_m represent the hydrodynamic dispersion coefficients of dissolved hydrogen and microbes, respectively; v_w is the Darcy flow velocity for the aqueous phase; and R_{H_2} and R_m represent the reaction source terms for dissolved hydrogen and microbes, respectively, which can be defined in the following forms:

$$R_{H_2} = \xi\left(p_g - H_c C_{H_2}\right) \Big/ M_{H_2} - \frac{1}{Y} \bullet \frac{C_m}{K_{m/s} + C_m} \tag{20}$$

$$R_m = -(k_1 + k_3)\varnothing_f S_w C_m + k_2 \rho_m \varnothing_1 + (g_1 - d_1)\varnothing_f S_w C_m \tag{21}$$

where M_{H_2} is the molar mass of hydrogen, k_1 is the reversible microbial adsorption rate, k_3 is the irreversible microbial adsorption rate, k_2 is the microbial desorption rate, ρ_m is the microbial density, $\varnothing_1$ is the volumetric fraction of microbes adsorbed reversibly on pore surface, g_1 is the microbial growth rate, and d_1 is the microbial decay rate. Here, more explanation is given for these two reaction source terms. The two terms on the right-hand side of Eq. (20) represent hydrogen transfer from gaseous phase to aqueous phase and the consumption of hydrogen induced by chemical reaction, respectively. The three terms on the right-hand side of Eq. (21) represent microbial adsorption on pore surface, microbial desorption from pore surface, and microbial growth and decay, respectively.

The microbial growth rate can be defined by the double Monod model with hydrogen and Fe_2O_3 serving as the limited substrates [30,41]:

$$g_1 = g_{1\,max} \bullet \frac{C_{H_2}}{K_{H_2/s} + C_{H_2}} \bullet \frac{C_{Fe_2O_3}}{K_{Fe_2O_3/s} + C_{Fe_2O_3}} \tag{22}$$

where $g_{1\,max}$ is the maximum microbial growth rate, $C_{Fe_2O_3}$ is the Fe_2O_3 concentration in porous rock, and $K_{H_2/s}$ and $K_{Fe_2O_3/s}$ are the half saturation constants for microbial growth. From the double Monod model, it can be known that the microbial growth rate is controlled by both the concentration of dissolved hydrogen in the aqueous phase and the concentration of Fe_2O_3 in porous rock.

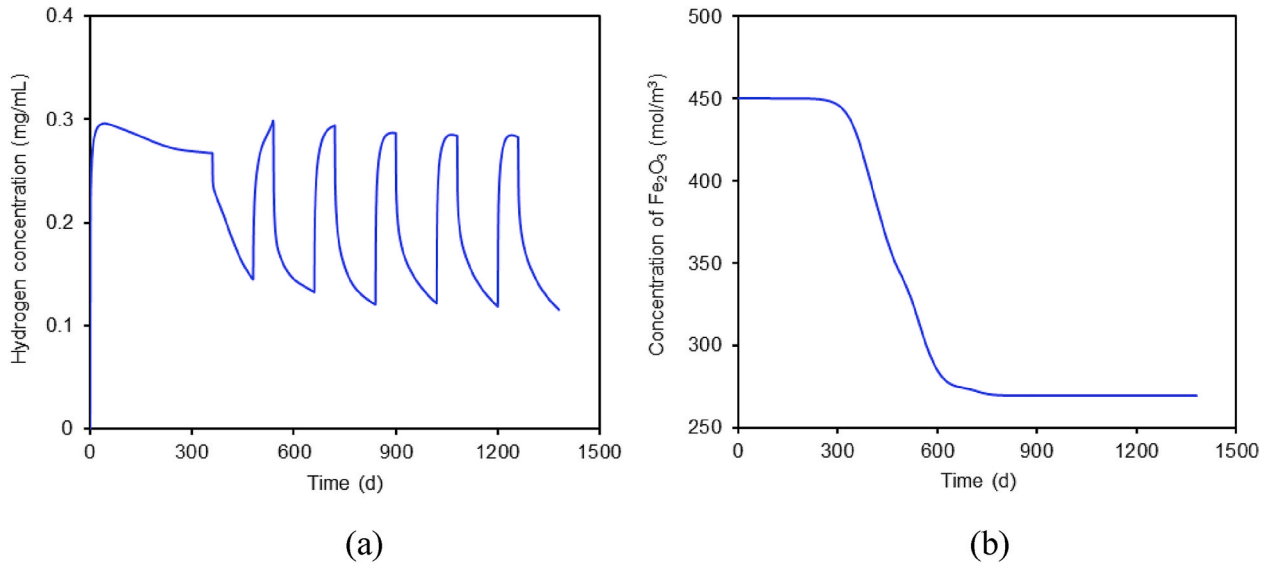

Fig. 10. Simulation results at the observation point: (a) variation of hydrogen concentration in formation water during cyclic hydrogen injection and withdrawal; (b) variation of Fe_2O_3 concentration during cyclic hydrogen injection and withdrawal.

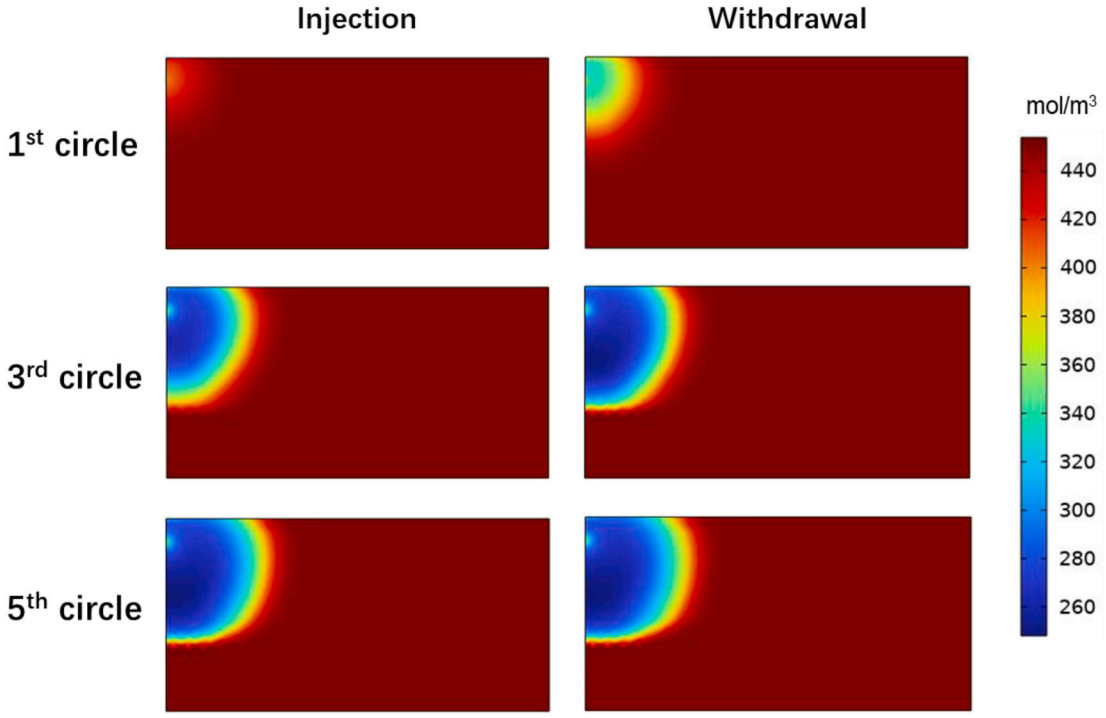

Fig. 11. Distribution of Fe_2O_3 concentration in porous rock at the end of different injection and withdrawal cycles.

3.4. Minerals dissolution and precipitation

As the iron reduction process leads to the dissolution of Fe_2O_3 and precipitation of Fe_3O_4, the mineral concentration in porous rock changes as well. The mass conservation equations for Fe_2O_3 and Fe_3O_4 can then be defined as:

$$\frac{\partial\left[(1-\varnothing)C_{Fe_2O_3}\right]}{\partial t}=R_{Fe_2O_3} \tag{23}$$

$$\frac{\partial\left[(1-\varnothing)C_{Fe_3O_4}\right]}{\partial t}=R_{Fe_3O_4} \tag{24}$$

where $C_{Fe_3O_4}$ is the Fe_3O_4 concentration in porous rock, and $R_{Fe_2O_3}$ and $R_{Fe_3O_4}$ are the reaction source terms for Fe_2O_3 and Fe_3O_4, respectively, which can be expressed in the following forms:

$$R_{Fe_2O_3}=-3\bullet\frac{1}{Y}\bullet\frac{C_m}{K_{m/s}+C_m} \tag{25}$$

$$R_{Fe_3O_4}=2\bullet\frac{1}{Y}\bullet\frac{C_m}{K_{m/s}+C_m} \tag{26}$$

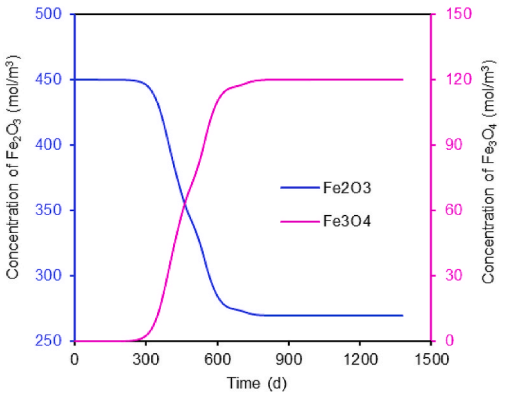

Fig. 12. Variation of Fe_2O_3 and Fe_3O_4 concentrations at the observation point during cyclic hydrogen injection and withdrawal.

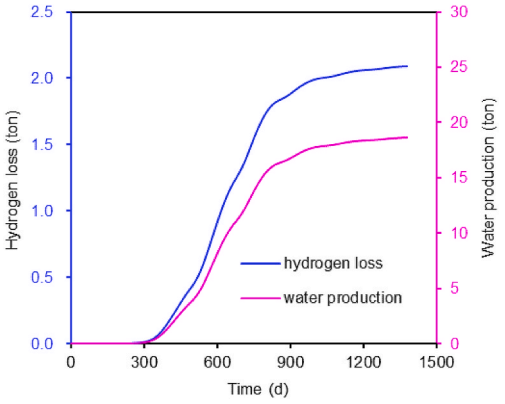

Fig. 13. Cumulative hydrogen loss and water production in aquifer during cyclic hydrogen injection and withdrawal.

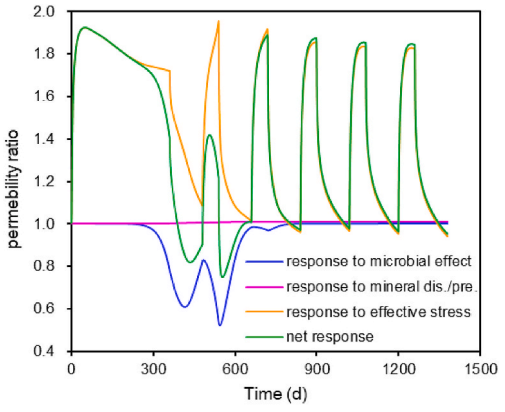

Fig. 14. Evolution of rock permeability at the observation point during cyclic hydrogen injection and withdrawal.

3.5. Microbial activities

During UHS, microbial growth is stimulated by the elevation of hydrogen concentration in the aqueous phase. Many studies have suggested that the microbial growth can lead to bioclogging of the pore system with subsequent changes in porosity and permeability of the porous media. From the traditional point of view, the distribution of microbes in porous media is assumed to be in the form of biofilm covering the surface of the grain particles. Based on this assumption, bioclogging induced porosity change can be attributed to the volumetric fraction of microbes adsorbed on the pore surface and to the subsequent growth of this biofilm [39,42,43]. In this work, we also make the assumption that those microbes suspended in the aqueous phase doesn't make contribution to the change of rock porosity. According to the above two assumptions, the mass conservation equations for microbes adsorbed reversibly and irreversibly on pore surface can be defined as:

$$\frac{\partial(\rho_m \varnothing_1)}{\partial t} = k_1 \varnothing_f S_w C_m - k_2 \rho_m \varnothing_1 + g_1 \rho_m \varnothing_1 - d_1 \rho_m \varnothing_1 \tag{27}$$

$$\frac{\partial(\rho_m \varnothing_2)}{\partial t} = k_3 \varnothing_f S_w C_m + g_1 \rho_m \varnothing_2 - d_1 \rho_m \varnothing_2 \tag{28}$$

From the above two equations, it can be known that microbial activities in pore system involve microbial adsorption/desorption and microbial growth/decay. Further, microbial adsorption includes reversible microbial adsorption and irreversible microbial adsorption.

3.6. Rock porosity and permeability

In this section, rock porosity and permeability models are developed. Considering a porous medium containing the pore volume V_p and the bulk volume V, we can have the porosity $\varnothing$ as follows:

$$\varnothing = \frac{V_p}{V} \tag{29}$$

Then, the porosity change can be expressed as:

$$d\varnothing = d\left(\frac{V_p}{V}\right) = \frac{V_p}{V}\left(\frac{dV_p}{V_p} - \frac{dV}{V}\right) \tag{30}$$

Substituting Eq. (29) into Eq. (30) and rearranging, we can obtain:

$$\frac{d\varnothing}{\varnothing} = \frac{dV_p}{V_p} - \frac{dV}{V} \tag{31}$$

The terms on the right-hand side of Eq. (31) represent the volumetric strains of pores and the rock, respectively. And these two strains can also be defined using the poroelasticity theory:

$$\frac{dV}{V} = -\frac{1}{K}(d\bar{\sigma} - \alpha dp) \tag{32}$$

$$\frac{dV_p}{V_p} = -\frac{1}{K_p}(d\bar{\sigma} - \beta dp) \tag{33}$$

where $\alpha = 1 - K/K_s$ and $\beta = 1 - K_p/K_s$ are the Biot coefficients of the rock and the pores, respectively; K, K_p and K_s represent the bulk modulus of the rock, the pores and the grains, respectively; and $\bar{\sigma} = -(\sigma_{11} + \sigma_{22} + \sigma_{33})/3$ is the mean stress.

Substituting Eqs. (32) and (33) into Eq. (31), the following relation can be derived:

$$\frac{d\varnothing}{\varnothing} = \left(\frac{1}{K} - \frac{1}{K_p}\right)(d\bar{\sigma} - dp) \tag{34}$$

Assuming the constant K and K_p, integrating the above equation with time yields:

$$\varnothing = \varnothing_0 \, exp\left\{\left(\frac{1}{K} - \frac{1}{K_p}\right)[(\bar{\sigma} - \bar{\sigma}_0) - (p - p_0)]\right\} \tag{35}$$

where the subscript "0" denotes the parameter value at the initial state. As the value of K is commonly several orders of magnitude larger than the value of K_p, we can have the simplification $\frac{1}{K} - \frac{1}{K_p} \approx -\frac{1}{K_p}$. Further, $\frac{1}{K_p}$ can be defined as the compressibility of pores. Then, we can have the relation between porosity and effective stress:

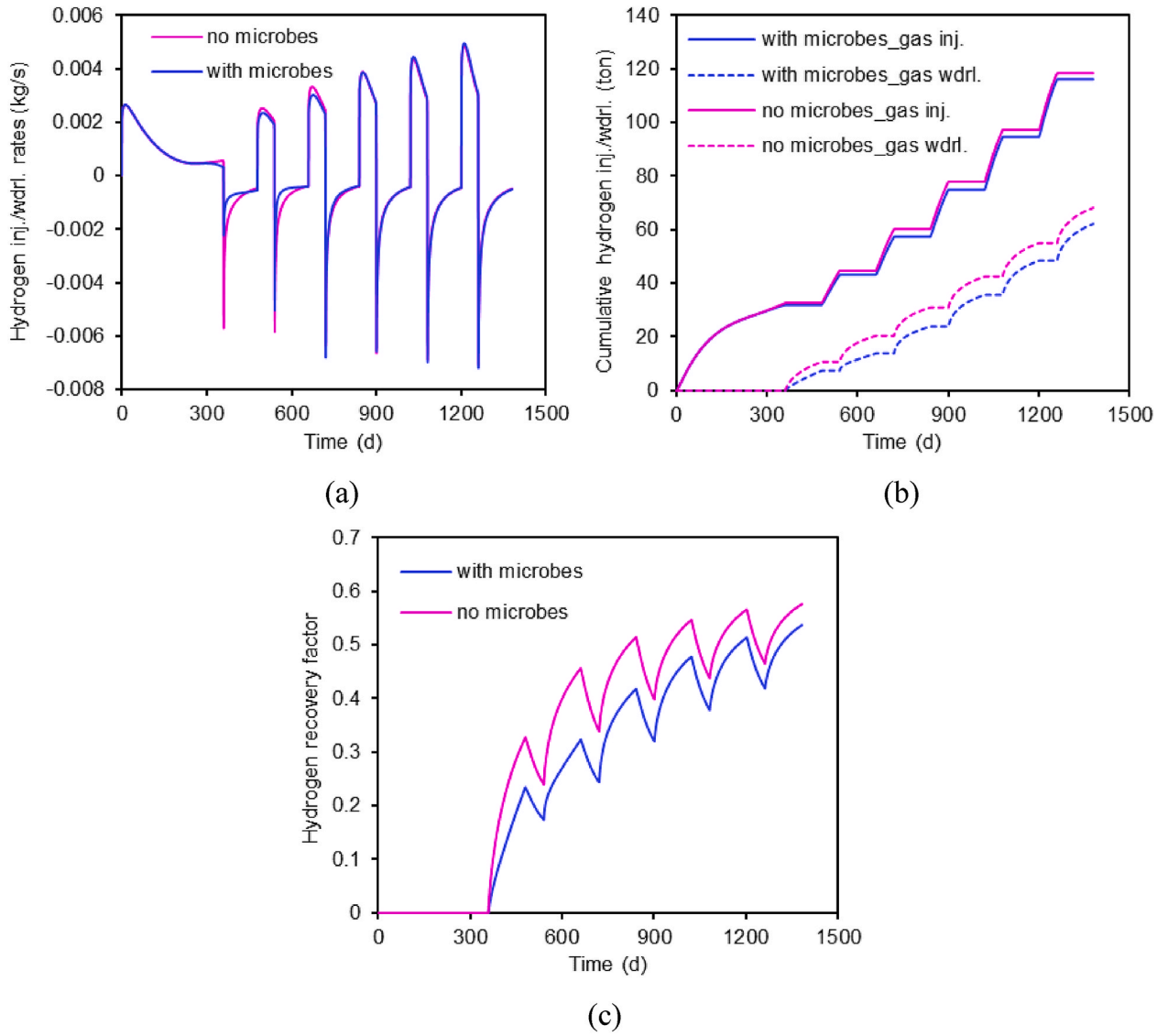

Fig. 15. Simulation results: (a) variation of hydrogen injection and withdrawal rates; (b) cumulative hydrogen injected and withdrawn; (c) variation of hydrogen recovery factor.

$$\varnothing = \varnothing_0 \, exp\{ -c_p[(\bar{\sigma} - \bar{\sigma}_0) - (p - p_0)]\} \tag{36}$$

where $c_p = \frac{1}{K_p}$ represents pore compressibility.

As rock porosity changes under the joint impacts of effective stress, microbial clogging and mineral dissolution/precipitation, the final form of porosity model can be expressed as below:

$$\varnothing = \varnothing_0 \, exp\{ -c_p[(\bar{\sigma} - \bar{\sigma}_0) - (p - p_0)]\} - \varnothing_{bc} + \varnothing_d - \varnothing_p \tag{37}$$

where $\varnothing_{bc} = \varnothing_1 + \varnothing_2$ is the porosity change induced by microbial clogging; and $\varnothing_d$ and $\varnothing_p$ are the porosity change induced by mineral dissolution and precipitation, respectively, which can be defined as follows:

$$\varnothing_d = \frac{\Delta C_{Fe_2O_3} M_{Fe_2O_3}}{\rho_{rock}} \tag{38}$$

$$\varnothing_p = \frac{\Delta C_{Fe_3O_4} M_{Fe_3O_4}}{\rho_{rock}} \tag{39}$$

where $\Delta C_{Fe_2O_3}$ and $\Delta C_{Fe_3O_4}$ represent the change of Fe_2O_3 and Fe_3O_4 concentrations in rock, respectively; $M_{Fe_2O_3}$ and $M_{Fe_3O_4}$ represent the molar mass of Fe_2O_3 and Fe_3O_4, respectively; and ρ_{rock} is the rock density.

Finally, rock permeability can be derived applying the Kozeny law [44]:

$$k = \frac{\varnothing^3}{c\tau^2 S^2} \tag{40}$$

where c is the Kozeny constant that depends on the geometry of the porous media, τ is the tortuosity of the porous media, and S is the pore surface area per unit volume.

3.7. Cross coupling relations

As can be summarized here, rock geomechanical deformation is defined by Eq. (5). Water-hydrogen two-phase flow is defined by Eqs. (7) and (8). Multispecies reactive transport are defined by Eqs. (18) and (19). Minerals dissolution and precipitation are defined by Eqs. (23) and (24). Microbial adsorption/desorption and growth/decay are defined by Eqs. (27) and (28). The interactions and coupling relations of all these processes are depicted in Fig. 2. As can be seen, rock deformation impacts fluid flow through changing porosity and permeability. Fluid flow

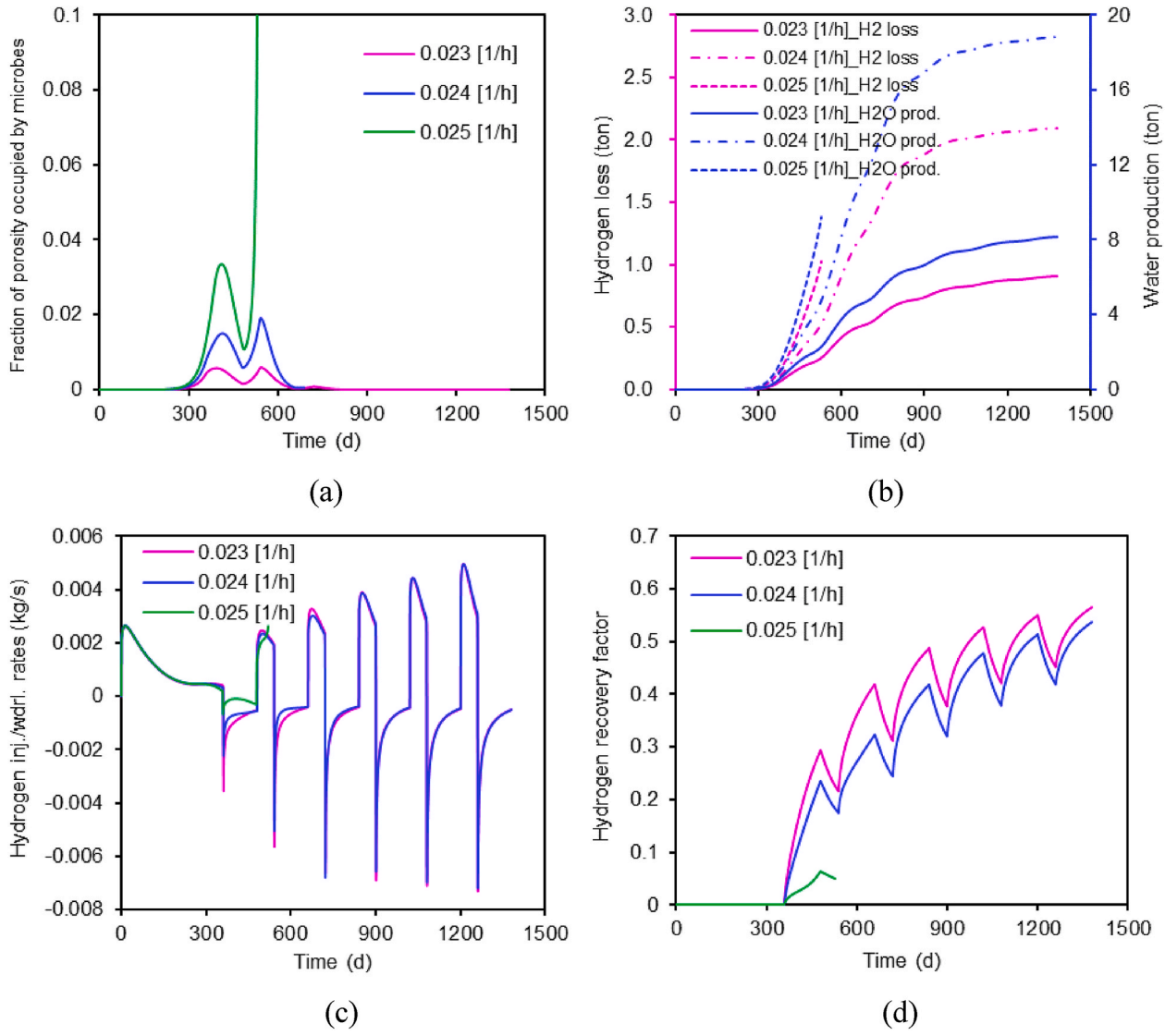

Fig. 16. Impact of microbial growth rate on: (a) adsorbed microbe population at the observation point; (b) cumulative hydrogen loss and water production; (c) hydrogen injection and withdrawal rates; and (d) hydrogen recovery factor.

impact rock deformation and reactive transport through changing effective stress and solutes advection-dispersion, respectively. Minerals dissolution and precipitation impact fluid flow through changing rock porosity and permeability while reactive transport impacts microbial activities through controlling microbial concentration and distribution. Microbial activities impact fluid flow, reactive transport and mineral dissolution/precipitation through microbial clogging of pore space, changing hydrogen consumption rate and mineral dissolution/precipitation rates, respectively.

4. Model verification

4.1. Model verification for chemical reaction between hydrogen and Fe (III) in rock

Since there is a lack of core flooding experiment data on chemical reaction between hydrogen and Fe(III) in rock, a zero-dimension problem is modeled here and the modeling results are compared with the batch reactor experiment data reported by Roden and Zachara [45]. In their experiment, goethite (source of Fe(III)) and hydrogen were collected for the chemical reaction. Goethite serves as the sole electron acceptor and hydrogen serves as the sole electron donor. The goethite-hydrogen medium was first filled into a 100 mL culture bottle with goethite concentration being 500 mmol/L and hydrogen volume being 30 mL. The goethite-hydrogen medium also contained 10 mM malate as the carbon source (but not the electron donor) for microbial growth. Then, BrY cells (the microbe) were added into the bottle to catalyze the redox reaction. The experiment was conducted at the static condition with the temperature remaining at 35 °C. The whole experiment lasts for 18 days. During this period, samples for Fe(II) and BrY cells were collected at a 2–4 days interval and the concentrations of the collected samples were measured. As the experimental techniques used to measure microbial and Fe(II) concentrations are complicated and beyond the scope of this work, the detailed introduction of these techniques will not be included in here. Readers who are interested can read the Analytical Techniques section of the literature published by Roden and Zachara [45]. It should also be noted here that the chemical reaction involved in the experiment by Roden and Zachara [45] is not exactly the same as the chemical reaction described by Eq. (1), but verifying our model against this experiment data is still necessary as both these reactions involve hydrogen oxidation and Fe(III) reduction.

To model the variation of Fe(II) concentration and microbial concentration in the batch reactor environment, the partial differential equations of the proposed multiphysics model were reduced to the

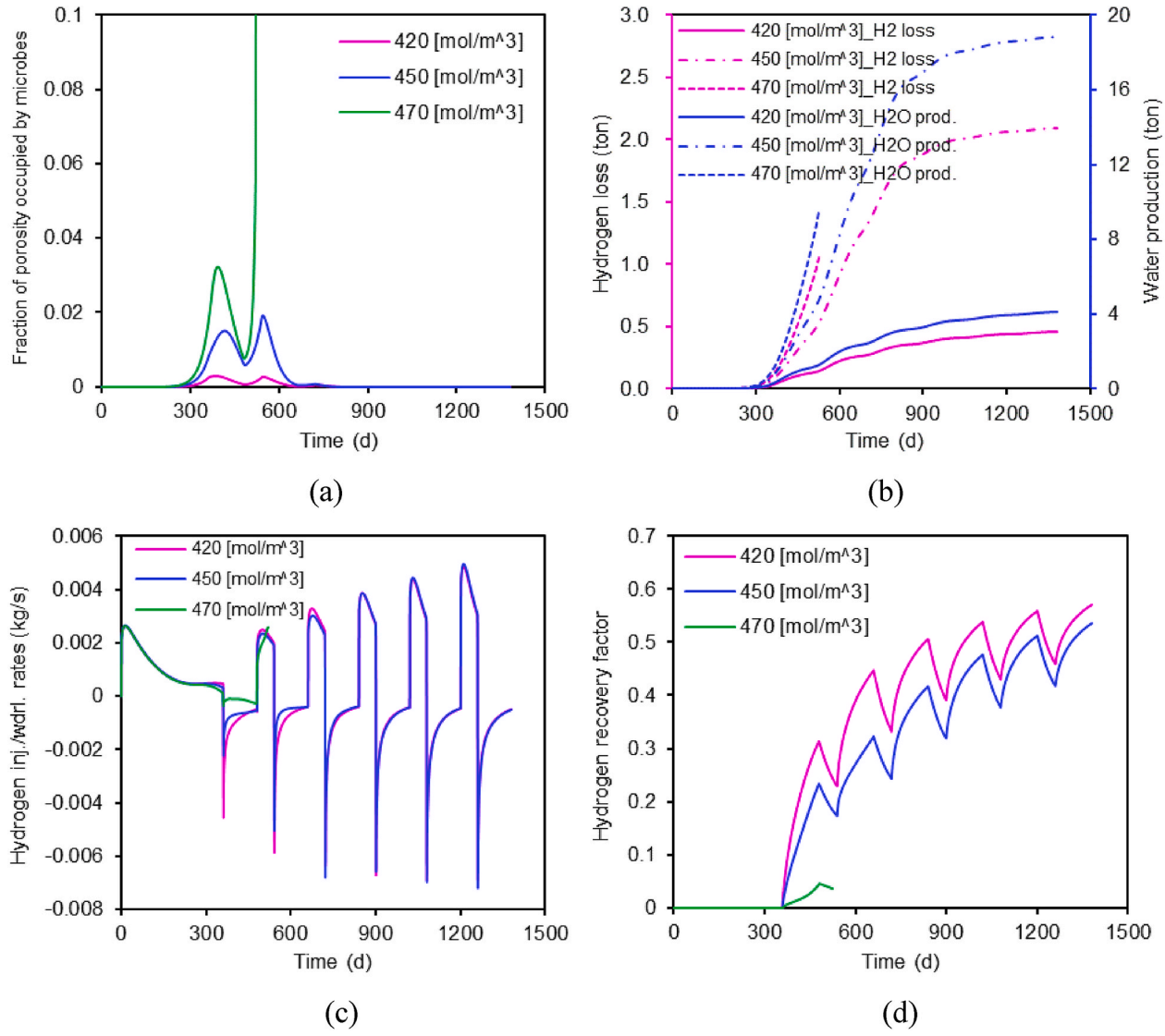

Fig. 17. Impact of initial Fe_2O_3 concentration on: (a) adsorbed microbe population at the observation point; (b) cumulative hydrogen loss and water production; (c) hydrogen injection and withdrawal rates; and (d) hydrogen recovery factor.

ordinary differential equations. Applying the ordinary differential equations and the parameters listed in Table 1, the variation of Fe(II) concentration and microbial concentration can be calculated, see Fig. 3. From this figure, it can be found that our modeling results can match the experimental data in a good manner. For further observation, it can be known that microbial concentration increases in the first week. This is because substrates are rich enough in this stage to support microbial growth [36]. Correspondingly, Fe(II) concentration exponentially increases. One week later, microbial concentration starts to decline. This is because substrates for microbial growth are gradually consumed and thus microbial decay outcompetes microbial growth in this period. Correspondingly, the increase of Fe(II) concentration slows down and remains almost unchanged in the end of the experiment.

4.2. Model verification for microbial transport and adsorption process

In this section, the model describing microbial transport and adsorption in porous media is verified through comparing the numerical results with the core flooding experiment data reported by Henry et al. [46]. In the experimental study, medium to coarse grained silica sand was used to create the sand column (5 cm in diameter and 40 cm in length). Sieve analysis shows that the sand size was in the range of 250–1000 μm in diameter. The porosity of the sand column was measured to be around 0.4. During the experiment, artificial ground water was used as the solution and constant bottom-to-top water flux of 6.6 cm^3/h was maintained through the long sand column. This water flux was equivalent to the linear velocity of 0.84 cm/h. In the first step, artificial ground water was flushed through the 40 cm long sand column for 192 h. Then, the water containing microbes with microbial concentration of 4.32 mg/L was introduced into the sand column for 38.4 h. After introducing the microbes, artificial ground water was flushed through the sand column once again for another 240 h. Effluent samples from the top side of the column were collected throughout the experiment to analyze microbial concentration in the effluent water. To make comparison between the modeling and experimental results, we also calculate the evolution of microbial concentration at the outlet of our numerical model. As the experimental data has a wide range of distribution, three different microbial growth rates as listed in Table 2 were used in our simulation. From Fig. 4, it can be known that the modelling results can cover the experiment data distribution area which implies that our model has the capability to describe the microbial transport and adsorption process in porous medium.

Here, more explanation is given on why microbial concentration decreases after reaching to a peak point and then increases. When

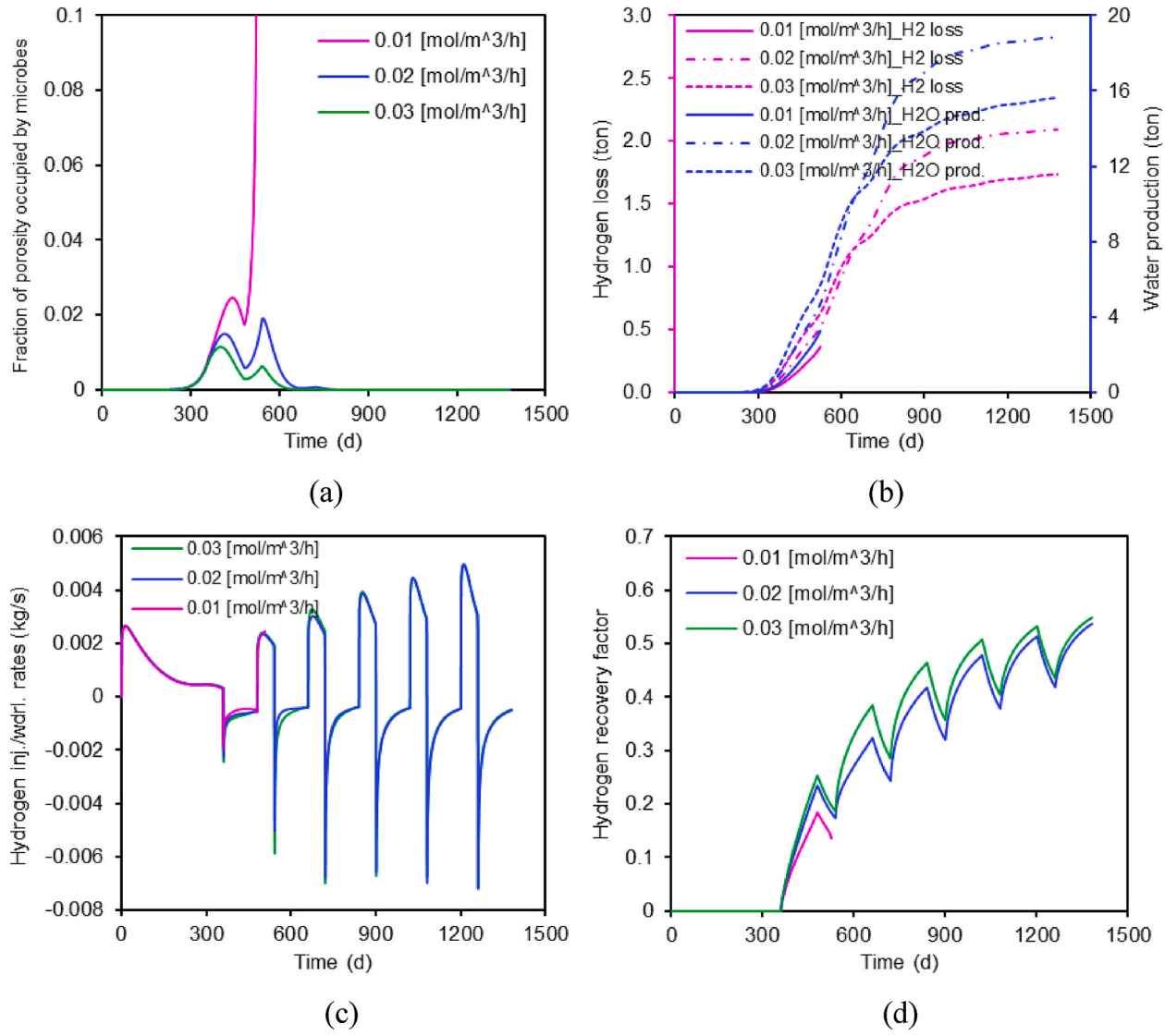

Fig. 18. Impact of Fe_2O_3 dissolution rate on: (a) adsorbed microbe population at the observation point; (b) cumulative hydrogen loss and water production; (c) hydrogen injection and withdrawal rates; and (d) hydrogen recovery factor.

artificial ground water was flushed into sand column to displace microbes out, microbial concentration in the effluent first rapidly increases from zero to a peak value in a very short time as great number of microbes have accumulated in core before the displacement. After reaching the peak value, microbial concentration in the effluent gradually decreases as microbes have been continuously displaced and microbial population in core decreases. With the progress of displacement, microbial concentration in the effluent switch from decreasing trend to increasing trend once again as in this period microbial growth starts to dominate microbial concentration in core.

5. Model applications and results analysis

In this section, the proposed HMCB multiphysics model is applied to investigate the impacts of microbial activities on UHS in aquifers. First, the geometry and initial and boundary conditions of the numerical model is introduced. Then, the numerical results of the base case are presented and analyzed. After that, parametric studies are performed to investigate the impacts of a series of parameters on UHS in aquifers. In each group of parametric study, only one input parameter is changed with all the other parameters kept identical to that of the base case unless otherwise specified. The investigated parameters include microbial growth rate, initial Fe_2O_3 concentration, Fe_2O_3 dissolution rate, injection pressure and withdrawal pressure.

5.1. Numerical model description

Fig. 5 shows the geometry of the numerical model that is used for modeling UHS in aquifer. Due to the symmetry, only a half of the aquifer is modeled. The length of the model is 500 m and the height is 250 m. The top surface of the model is located at the depth of 1000 m and the whole domain is assumed at an isothermal condition with the temperature remaining at 320 K. A horizontal wellbore (wellbore radius equals to 5 cm) that is perpendicular to this vertical plane is set on the left boundary of the model with the distance between the wellbore and the top surface of the aquifer being 30 m. The wellbore is used for both hydrogen injection and withdrawal. To evaluate the dynamic responses of reservoir properties during UHS, an observation point is set near the wellbore with the horizontal distance between the observation point and the wellbore being 30 m as well.

For initial conditions, the pore space of aquifer is assumed initially 100% filled by the formation water. Also, the aquifer is assumed initially under the hydrostatic pressure conditions. In addition, the initial hydrogen concentration and microbial concentration in the aqueous

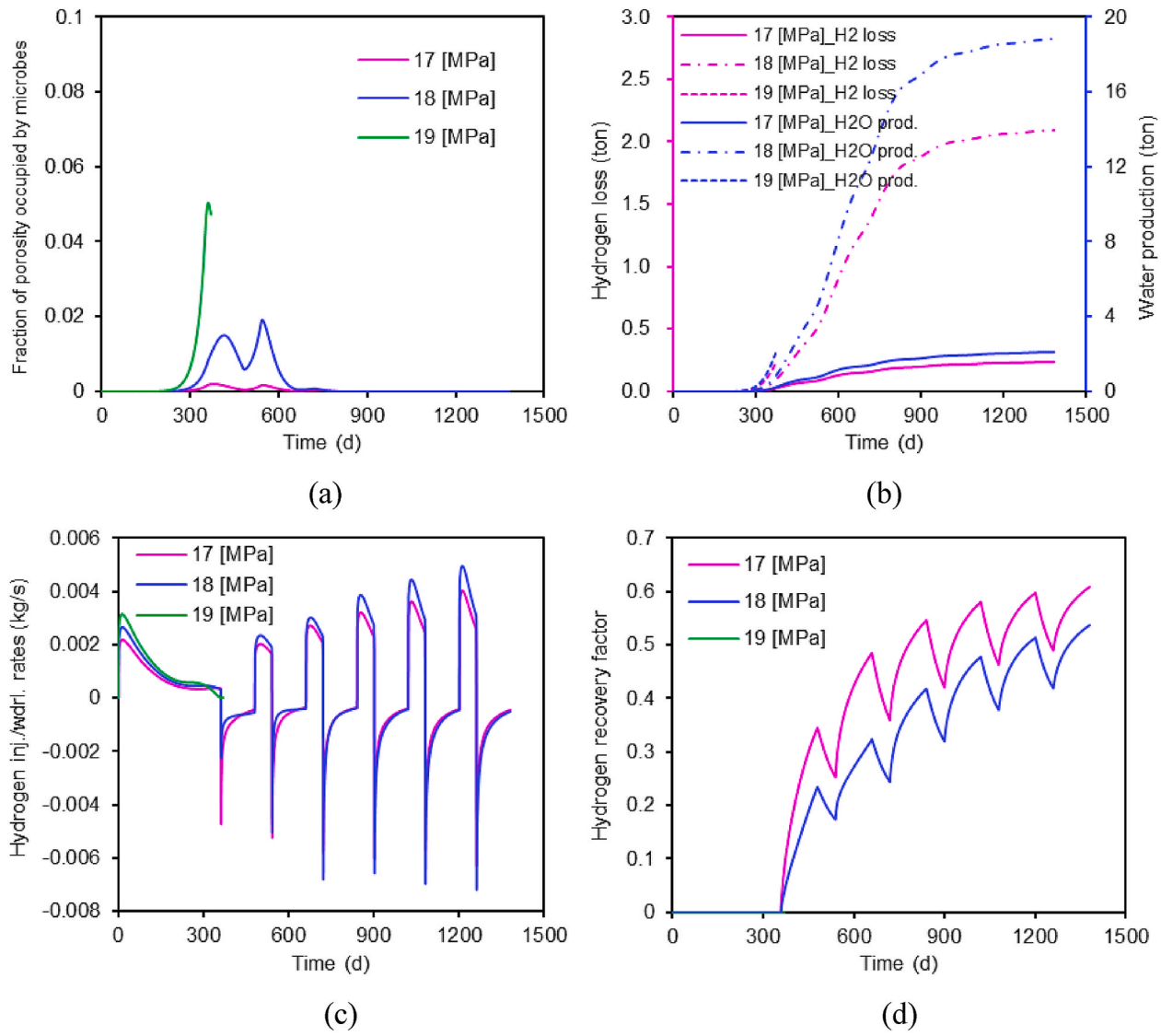

Fig. 19. Impact of injection pressure on: (a) adsorbed microbe population at the observation point; (b) cumulative hydrogen loss and water production; (c) hydrogen injection and withdrawal rates; and (d) hydrogen recovery factor.

phase, the initial Fe_2O_3 and Fe_3O_4 concentration in the rock, and the initial volumetric fraction of microbes adsorbed on the pore surface are set.

For boundary conditions, the normal displacements of the left and bottom boundaries are restricted to zero and the confining pressure is applied to the top and right boundaries. Meanwhile, the top, right and bottom boundaries are considered as impervious which means that no flow/flux is allowed through these boundaries [47]. During UHS, constant injection pressure and withdrawal pressure are applied on the wellbore wall.

In our simulation, a certain amount of cushion gas (hydrogen in this work) is first injected into the aquifer for 10 months with the purpose of maintaining the operation pressure. Then during the storage operation, hydrogen is first injected into the aquifer for two months and then withdrawn from the aquifer for four months in each cycle. Totally, six storage cycles are simulated. In each cycle, the hydrogen injection pressure is kept as 18 MPa and the withdrawn pressure is kept as 8 MPa. All the input parameters involved in the numerical simulation for the base case are summarized in Table 3.

5.2. *Simulation results for the base case*

Fig. 6 shows the temporal evolution of hydrogen saturation in aquifer during repeated hydrogen injection and withdrawal cycles. As can be seen, hydrogen tends to migrate upwards and then accumulates at the top surface of the aquifer. This is mainly because the density of hydrogen is much smaller than the density of formation water and thus buoyant flow, which is caused by gravitational force, plays a significant role during hydrogen migration [48,49]. With the increase of injection and withdrawal cycles, the hydrogen saturation at the top surface gradually increases which means that more and more hydrogen accumulates at the top of the storage aquifer with the progress of UHS. This finding implies that the production well should be placed at the upper part of the storage aquifer instead of the lower part in terms of enhancing hydrogen recovery. Fig. 7 shows the variation of hydrogen saturation at the observation point. From this figure, it can be known that hydrogen saturation increases in the injection phase while decreases in the withdrawal phase. Overall, hydrogen saturation exhibits an increasing trend with the progress of UHS.

Figs. 8 and 9 show the temporal evolution of adsorbed microbe population in the aquifer and at the observation point during repeated hydrogen injection and withdrawal cycles, respectively. The value of

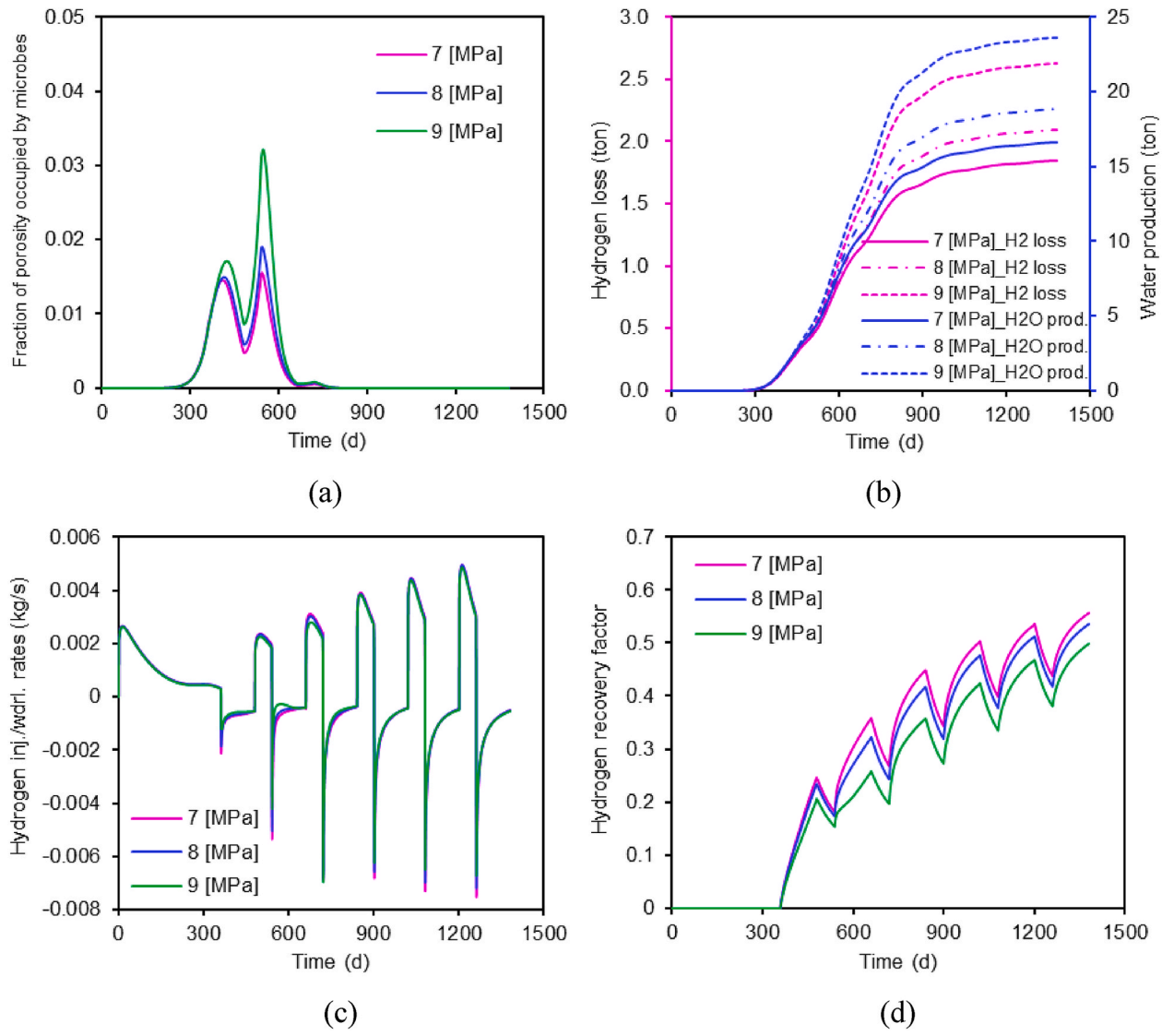

Fig. 20. Impact of withdrawal pressure on: (a) adsorbed microbe population at the observation point; (b) cumulative hydrogen loss and water production; (c) hydrogen injection and withdrawal rates; and (d) hydrogen recovery factor.

these two figures represents the fraction of porosity occupied by those microbes attached on the pore surface. The larger the value, the greater the microbe population. As can be seen, microbes distribute surrounding the wellbore instead of at the top surface of the aquifer. This is mainly because injection pressure is applied at wellbore and thus the dissolved hydrogen concentration surrounding the wellbore is the greatest which stimulates microbial activities in this region the most. It can also be found that microbe population on pore surface increases during hydrogen injection while declines during hydrogen withdrawal as the hydrogen concentration in formation water (see Fig. 10(a)) periodically changes with reservoir pressure during UHS. For further observation, it can be found that the microbes almost die out after three cycles of hydrogen injection and withdrawal. This is mainly attributed to the dissolution of Fe_2O_3 during UHS, see Fig. 10(b). The dissolution of Fe_2O_3 leads to the decrease of microbial growth rate (see Eq. (22)). Thus, the net microbial growth rate decreases in the increased cycle of hydrogen injection while the net microbial decay rate increases in the increased cycle of hydrogen withdrawal. This is the primary reason why microbes die out after three cycles of UHS.

Fig. 11 shows the temporal evolution of Fe_2O_3 concentration in porous rock during repeated hydrogen injection and withdrawal cycles. As can be seen, the area where Fe_2O_3 dissolves gradually enlarges during UHS and this area is consistent with the area where microbes distribute (see Fig. 8). Fig. 12 shows the variation of Fe_2O_3 and Fe_3O_4 concentrations at the observation point. As iron reduction process leads to Fe_2O_3 dissolution and Fe_3O_4 precipitation, correspondingly the concentration of Fe_2O_3 decreases and the concentration of Fe_3O_4 increases. Fig. 13 shows the cumulative hydrogen loss and water production during iron reduction process. The total water production is around 18.5 ton and the total hydrogen loss is around 2.1 ton which is less than 2% of the total hydrogen injected during the six cycles of UHS.

Fig. 14 shows the rock permeability evolution at the observation point during UHS. In this work, we consider the joint impacts of microbial clogging, mineral dissolution and precipitation, and effective stress change on permeability evolution. As can be seen, microbial clogging leads to permeability decline during UHS and its impact can be ignored after three cycles of hydrogen injection and withdrawal. For mineral dissolution and precipitation, the permeability increase induced by Fe_2O_3 dissolution is nearly counteracted by the permeability decline induced by Fe_3O_4 precipitation. Thus, the impact of mineral dissolution and precipitation can be neglected during UHS. For effective stress, its impact on aquifer permeability is the most significant and lasts during the whole UHS operations.

Fig. 15(a) shows the variation of hydrogen injection and withdrawal

rates during the six repeated cycles. Notet that the positive value in this figure represents injection rate while the negative value represents withdrawal rate. The results for the case that does not consider the impacts of microbial activities are also presented for a reference. As can be seen, the inclusion of microbial activities leads to the decline of hydrogen injection and withdrawal rates in the first three cycles. This phenomenon can be explained from three aspects. First, microbial clogging results in permeability decline which lowers hydrogen injection and withdrawal rates. Second, water production during iron reduction process decreases hydrogen saturation and relative permeability, thus leading to the reduction of hydrogen injection and withdrawal rates. Third, the iron reduction process induces permanent hydrogen loss. Fig. 15(b) shows the cumulative hydrogen injected and withdrawn. It can be seen that both the amounts of injected and withdrawn hydrogen decrease when the impacts of microbial activities are considered with the amount of hydrogen withdrawn decreasing more than the amount of hydrogen injected. Fig. 15(c) shows the variation of hydrogen recovery factor during UHS. The recovery factor is defined as the ratio of cumulative hydrogen withdrawn to cumulative hydrogen injected. As can be seen, hydrogen recovery factor declines when the impacts of microbial activities are considered.

5.3. Parametric studies

The investigated five parameters can be classified into two categories. The first category includes microbial growth rate, initial Fe_2O_3 concentration and Fe_2O_3 dissolution rate which are all biochemical parameters. The second category includes injection pressure and withdrawal pressure which are operational parameters. In the following, the impact of each parameter on UHS in aquifers is analyzed.

5.3.1. The impact of microbial growth rate

In this subsection, we investigate the impact of microbial growth rate on UHS in aquifers. From Fig. 16(a), it can be found that the increase of microbial growth rate leads to more severe bioclogging. When g_1 reaches 0.025 1/h, pore space is fully occupied by microbes. In this case, permeability declines to zero and subsequent hydrogen injection and withdrawal cannot proceed. From Fig. 16(b), it can be known that more hydrogen is lost and more water is produced when microbial growth rate increases. As larger microbial growth rate leads to more severe bioclogging, more hydrogen loss and more water production, the hydrogen injection and withdrawal rates decrease thereby, as shown in Fig. 16(c). From Fig. 16(d), it can also be known that hydrogen recovery factor declines with the increase of microbial growth rate.

5.3.2. The impact of initial Fe_2O_3 concentration

In this subsection, we investigate the impact of initial Fe_2O_3 concentration on UHS in aquifers. According to Eq. (22), the larger the Fe_2O_3 concentration, the greater the microbial growth rate. Therefore, it can be found from Fig. 17(a) that the increase of initial Fe_2O_3 concentration leads to more severe bioclogging. When initial Fe_2O_3 concentration reaches 470 mol/m^3, pore space is fully clogged by microbes. In this case, subsequent hydrogen injection and withdrawal cannot proceed. From Fig. 17(b), the larger initial Fe_2O_3 concentration leads to more hydrogen loss and more water production during iron reduction process. As larger initial Fe_2O_3 concentration leads to more severe bioclogging, more hydrogen loss and more water production, lower hydrogen injection and withdrawal rates are observed thereby, see Fig. 17(c). From Fig. 17(d), it can be found that hydrogen recovery factor declines with the increase of initial Fe_2O_3 concentration.

5.3.3. The impact of Fe_2O_3 dissolution rate

In this subsection, we investigate the impact of Fe_2O_3 dissolution rate on UHS in aquifers. The smaller the Fe_2O_3 dissolution rate, the slower the microbial growth rate decreases. Therefore, the bioclogging phenomenon becomes more severe when Fe_2O_3 dissolution rate decreases, as shown in Fig. 18(a). When Fe_2O_3 dissolution rate decreases to 0.01 mol/m^3/h, pore space is fully bioclogged which hinders the subsequent hydrogen injection and withdrawal. From Fig. 18(b), more hydrogen is lost and more water is produced with the decrease of Fe_2O_3 dissolution rate. As smaller Fe_2O_3 dissolution rate leads to more severe bioclogging and more hydrogen loss and water production, lower hydrogen injection and withdrawal rates are observed thereby, as shown in Fig. 18(c). In Fig. 18(d), it can be found that hydrogen recovery factor declines with the decrease of Fe_2O_3 dissolution rate.

5.3.4. The impact of injection pressure

In this subsection, we investigate the impact of injection pressure on UHS in aquifers. According to Eq. (22), the microbial growth rate is directly proportional to hydrogen concentration in formation water. As larger injection pressure leads to more hydrogen dissolved in formation water, the microbial growth rate becomes greater with the increase of injection pressure. From Fig. 19(a), the bioclogging phenomenon becomes more severe with the increase of injection pressure. When injection pressure reaches 19 MPa, pore space is fully bioclogged (not at the observation point but at the area more close to the wellbore) and hydrogen cannot be further injected and withdrawn in this case. From Fig. 19(b), more hydrogen is lost and more water is produced when injection pressure increases. As larger injection pressure leads to more severe bioclogging, more hydrogen loss and more water production, lower hydrogen injection and withdrawal rates are yielded thereby, see Fig. 19(c). From Fig. 19(d), hydrogen recovery factor decreases when injection pressure increases.

5.3.5. The impact of withdrawal pressure

In this subsection, we investigate the impact of withdrawal pressure on UHS in aquifers. When withdrawal pressure is lowered, more hydrogen will be released from formation water during withdrawal phase which will lead to the decrease of microbial growth rate. Therefore, the greater the withdrawal pressure is, the more severe the bioclogging phenomenon will be, as shown in Fig. 20(a). Also, it can be observed from Fig. 20(b) that the larger withdrawal pressure leads to more hydrogen loss and more water production during iron reduction process. As larger withdrawal pressure leads to more severe bioclogging, more hydrogen loss and more water production, hydrogen injection and withdrawal rates are lowered thereby, see Fig. 20(c). From Fig. 20(d), hydrogen recovery factor decreases with the increase of withdrawal pressure.

6. Conclusions

In this work, we propose a coupled HMCB multiphysics model to investigate the impacts of IRB activities on UHS in aquifers. This multiphysics model couples (1) rock deformation; (2) water-hydrogen two-phase flow; (3) microbes and dissolved hydrogen transport; (4) mineral dissolution/precipitation; and (5) microbial adsorption/desorption and growth/decay together. Based on the modelling results, the following conclusions can be drawn.

(1) Although hydrogen saturation at the top surface of the aquifer is the greatest, microbial activities surrounding the injection well is stimulated the most. As a result, the microbially clogged area and biochemical reactions occurring area surround the injection well as well.
(2) Microbial activities influence the initial few cycles of hydrogen injection and withdrawal. When hydrogen is injected into the aquifers, IRB activities are stimulated which catalyze the reaction between hydrogen and the mineral Fe_2O_3 in the hosting rock. In this process, the concentration of Fe_2O_3 in rock decreases and thereby microbial net growth rate declines and be negative until all microbes die out. Once microbes die out, the impacts of microbial activities on UHS operations disappear.

(3) Microbial activities can degrade hydrogen recovery efficiency through microbial clogging of pores, hydrogen consumption and water production. In comparison with hydrogen consumption and water production, microbial clogging affects UHS more significantly as aquifer pore space can be fully clogged by these microbes, in which condition subsequent hydrogen injection and withdrawal operations have to be suspended. Thus, these extreme cases should be avoided when planning UHS projects.
(4) During UHS, aquifer permeability dynamically changes under the joint impacts of microbial clogging, mineral dissolution/precipitation and effective stress. Among these three factors, effective stress plays the dominant role and controls aquifer permeability throughout the UHS operations, while microbial clogging only influences aquifer permeability in the initial few cycles of hydrogen injection and withdrawal. For mineral dissolution and precipitation, their impacts are counteracted and can be neglected.

The multiphysics model proposed in this work has general applicability. It can be used to evaluate hydrogen storage performance and screen projects in different types of reservoirs where microbes inhabit. When applying this model, certain parameters like microbial growth/decay rates, mineral concentrations, porosity/permeability and etc. need to be determined for a particular reservoir as underground environments vary greatly in different regions. In this research, the impact of IRB activities on UHS is investigated while co-existence of several different microbial species in reservoirs is possible and can thereby lead to more complex reactions and impacts on UHS. Modification of bio-reactive components of this multiphysics model can help to evaluate the joint impacts of these microbial species. In addition, the impacts of formation temperature and salinity on microbial activities are not considered in this work and these parameters may have significant impacts on microbial growth/decay and thereby influencing UHS. Future work should consider these factors.

CRediT authorship contribution statement

Qi Gao: Writing – original draft, Validation, Software, Methodology, Investigation, Funding acquisition, Conceptualization. **Jishan Liu:** Writing – review & editing, Supervision, Resources, Funding acquisition. **Derek Elsworth:** Writing – review & editing, Supervision, Conceptualization.

Declaration of competing interest

The authors declare that they have no known competing financial interests or personal relationships that could have appeared to influence the work reported in this paper.

Acknowledgements

This work is supported by the Australian Research Council under Grant DP200101293. The first author is also supported by the UWA-China Joint Scholarships (Grant No. 201906450050). These supports are gratefully acknowledged.

Appendix A

The Peng-Robin equation is used to model hydrogen density [49,50]:

$$p_g = \frac{RT}{V_{mg} - b} - \frac{a}{V_{mg}^2 + 2bV_{mg} - b^2} \tag{A1}$$

where T is temperature, V_{mg} is the molar volume of hydrogen, R is the universal gas constant, and a and b are the equation of state parameters. For pure components, a and b are expressed as a function of the critical pressure and temperature:

$$a = 0.45724 \frac{(RT_c)^2}{p_c} \bullet \left[1 + \kappa\left(1 - \sqrt{\frac{T}{T_c}}\right)\right]^2 \tag{A2}$$

$$b = 0.0778 \frac{RT_c}{p_c} \tag{A3}$$

$$\kappa = 0.37464 + 1.54226\omega - 0.26992\omega^2 \tag{A4}$$

where p_c is critical pressure, T_c is critical temperature, and κ is the acentric factor which can be determined by fitting the equation of state with the experimental hydrogen density data.

Appendix B

The Jossi, Stiel and Thodos equation is used to model hydrogen viscosity [49]:

$$\left[\left(\mu_g - \mu^*\right) \frac{T_c^{\frac{1}{6}}}{M_{H_2}^{\frac{1}{2}} p_c^{\frac{2}{3}}} + 10^{-4}\right]^{\frac{1}{4}} = a_0 + a_1\rho_r + a_2\rho_r^2 + a_3\rho_r^3 + a_4\rho_r^4 \tag{B1}$$

where μ_g is the viscosity of hydrogen, $\rho_r = \rho_g V_c$ is the reduced density, V_c is the critical volume of hydrogen, a_0, a_1, a_2, a_3 and a_4 are the fitting parameters, and μ^* is the low pressure viscosity for pure hydrogen [51]:

$$\mu^* \frac{T}{M_{H_2} p_c} = \left(4.610 \frac{T^{0.618}}{T_c} - 2.04e^{-0.449\frac{T}{T_c}} + 1.94e^{-4.058\frac{T}{T_c}} + 0.1\right) \times 10^{-4} \tag{B2}$$

Appendix C

The solubility of hydrogen in brine can be calculated by the following equation [52]:

$$\ln\left(\frac{x_{H_2}}{x^0_{H_2}}\right) = b_1 m^2_{NaCl} + b_2 m_{NaCl} \tag{C1}$$

where b_1 and b_2 are the fitting coefficients, m_{NaCl} is the salt concentration of brine, x_{H_2} is the hydrogen solubility in brine, and $x^0_{H_2}$ is the hydrogen solubility in pure water which is defined as a function of temperature and pressure:

$$x^0_{H_2} = c_1 pT + \frac{c_2 p}{T} + c_3 p + c_4 p^2 \tag{C2}$$

where c_1, c_2, c_3 and c_4 are the fitting coefficients. Here, it should be noted that the Eq. (C1) for hydrogen solubility in brine can be reduced to the Eq. (C2) for hydrogen solubility in pure water when salt concentration is equal to zero.

Using Eqs. (C1) and (C2), hydrogen solubility data under different pressure conditions can be calculated. Then, the corrected Henry's constant in Eq. (10) can be obtained through fitting the Henry's law with the calculated data.

References

[1] Herbert GMJ, et al. A review of wind energy technologies. Renew Sustain Energy Rev 2007;11(6):1117–45.
[2] Kannan N, Vakeesan D. Solar energy for future world:-A review. Renew Sustain Energy Rev 2016;62:1092–105.
[3] Chowdhury MS, et al. Current trends and prospects of tidal energy technology. Environ Dev Sustain 2021;23:8179–94.
[4] Jiang CZ, et al. Evolution of coal permeability during gas/energy storage. Int J Hydrogen Energy 2024;53:1373–86.
[5] Heinemann N, et al. Enabling large-scale hydrogen storage in porous media–the scientific challenges. Energy Environ Sci 2021;14(2):853–64.
[6] Gabrielli P, et al. Seasonal energy storage for zero-emissions multi-energy systems via underground hydrogen storage. Renew Sustain Energy Rev 2020;121:109629.
[7] Heidaryan E, Aryana SA. Empirical correlations for density, viscosity, and thermal conductivity of pure gaseous hydrogen. Adv Geo-Energy Res 2024;11(1):54–73.
[8] Caglayan DG, et al. Technical potential of salt caverns for hydrogen storage in Europe. Int J Hydrogen Energy 2020;45(11):6793–805.
[9] Raad SMJ, et al. Hydrogen storage in saline aquifers: opportunities and challenges. Renew Sustain Energy Rev 2022;168:112846.
[10] Okoroafor ER, et al. Toward underground hydrogen storage in porous media: reservoir engineering insights. Int J Hydrogen Energy 2022;47(79):33781–802.
[11] Hematpur H, et al. Review of underground hydrogen storage: concepts and challenges. Adv Geo-Energy Res 2023;7(2):111–31.
[12] Zeng L, et al. Storage integrity during underground hydrogen storage in depleted gas reservoirs. Earth Sci Rev 2023;247:104625.
[13] Wallace RL, et al. Utility-scale subsurface hydrogen storage: UK perspectives and technology. Int J Hydrogen Energy 2021;46(49):25137–59.
[14] Mahdi DS, et al. Hydrogen underground storage efficiency in a heterogeneous sandstone reservoir. Adv Geo-Energy Res 2021;5(4):437–43.
[15] Sambo C, et al. A review on worldwide underground hydrogen storage operating and potential fields. Int J Hydrogen Energy 2022;47(54):22840–80.
[16] Amirthan T, Perera MSA. Underground hydrogen storage in Australia: a review on the feasibility of geological sites. Int J Hydrogen Energy 2023;48(11):4300–28.
[17] Zeng L, et al. Role of geochemical reactions on caprock integrity during underground hydrogen storage. J Energy Storage 2023;65:107414.
[18] Pedrós-Alió C, Manrubia S. The vast unknown microbial biosphere. Proc Natl Acad Sci USA 2016;113(24):6585–7.
[19] Varjani SJ, Gnansounou E. Microbial dynamics in petroleum oilfields and their relationship with physiological properties of petroleum oil reservoirs. Bioresour Technol 2017;245:1258–65.
[20] Zivar D, et al. Underground hydrogen storage: a comprehensive review. Int J Hydrogen Energy 2021;46(45):23436–62.
[21] Navaid HB, et al. A comprehensive literature review on the challenges associated with underground hydrogen storage. Int J Hydrogen Energy 2023;48(28):10603–35.
[22] Amigáň P, et al. Methanogenic bacteria as a key factor involved in changes of town gas stored in an underground reservoir. FEMS (Fed Eur Microbiol Soc) Microbiol Ecol 1990;6(3):221–4.
[23] Pichler M. Underground sun storage results and outlook. In: EAGE/DGMK joint workshop on underground storage of hydrogen, vol. 2019. European Association of Geoscientists & Engineers; 2019. p. 1–4. 1.
[24] Hellerschmied C, et al. Hydrogen storage and geo-methanation in a depleted underground hydrocarbon reservoir. Nat Energy 2024;9:333–44.
[25] Pérez A, et al. Patagonia wind-hydrogen project: underground storage and methanation. In: 21st world hydrogen energy conference; 2016.
[26] Strobel G, et al. Coupled model for microbial growth and phase mass transfer in pressurized batch reactors in the context of underground hydrogen storage. Front Microbiol 2023;14:1150102.
[27] Khajooie S, et al. Methanogenic conversion of hydrogen to methane in reservoir rocks: an experimental study of microbial activity in water-filled pore space. Int J Hydrogen Energy 2024;50:272–90.
[28] Liu N, et al. Pore-scale study of microbial hydrogen consumption and wettability alteration during underground hydrogen storage. Front Energy Res 2023;11:1124621.
[29] Ebigbo A, et al. A coupled, pore-scale model for methanogenic microbial activity in underground hydrogen storage. Adv Water Resour 2013;61:74–85.
[30] Hagemann B, et al. Hydrogenization of underground storage of natural gas: impact of hydrogen on the hydrodynamic and bio-chemical behavior. Comput Geosci 2016;20:595–606.
[31] Eddaoui N, et al. Impact of pore clogging by bacteria on underground hydrogen storage. Transport Porous Media 2021;139:89–108.
[32] Dopffel N, et al. Microbial side effects of underground hydrogen storage–Knowledge gaps, risks and opportunities for successful implementation. Int J Hydrogen Energy 2021;46(12):8594–606.
[33] Kumari WGP, Ranjith PG. An overview of underground hydrogen storage with prospects and challenges for the Australian context. Geoenergy Sci Eng 2023;231:212354.
[34] Thaysen EM, et al. Estimating microbial growth and hydrogen consumption in hydrogen storage in porous media. Renew Sustain Energy Rev 2021;151:111481.
[35] Tian J, et al. Linking fractal theory to a fully coupled coal deformation and two-phase flow multiphysics: the role of fractal dimensions. Energy Fuels 2022;36(20):12591–605.
[36] Gao Q, et al. A multiphysics model for biogenic gas extraction from coal seams. Geoenergy Sci Eng 2023;228:212045.
[37] Szymkiewicz A. Modelling water flow in unsaturated porous media: accounting for nonlinear permeability and material heterogeneity. Springer Science & Business Media; 2012.
[38] Brooks RH, Corey AT. Properties of porous media affecting fluid flow. J Irrigat Drain Div 1966;92(2):61–88.
[39] Li J, et al. Interactions of microbial-enhanced oil recovery processes. Transport Porous Media 2011;87:77–104.
[40] Zhi S, et al. Hydraulic fracturing for improved nutrient delivery in microbially-enhanced coalbed-methane (MECBM) production. J Nat Gas Sci Eng 2018;60:294–311.
[41] Shojaee A, et al. Interplay between microbial activity and geochemical reactions during underground hydrogen storage in a seawater-rich formation. Int J Hydrogen Energy 2024;50:1529–41.
[42] Sivasankar P, Kumar GS. Influence of bio-clogging induced formation damage on performance of microbial enhanced oil recovery processes. Fuel 2019;236:100–9.
[43] Chakraborty S, et al. Numerical modeling on the influence of effective porosity, microbial kinetics, and operational parameters on enhanced oil recovery by microbial flooding within a sandstone formation. SPE J 2020;25(6):2932–61.
[44] Chen D, et al. A unified permeability and effective stress relationship for porous and fractured reservoir rocks. J Nat Gas Sci Eng 2016;29:401–12.
[45] Roden EE, Zachara JM. Microbial reduction of crystalline iron (III) oxides: influence of oxide surface area and potential for cell growth. Environ Sci Technol 1996;30(5):1618–28.
[46] Hendry MJ, et al. The role of sorption in the transport of Klebsiella oxytoca through saturated silica sand. Groundwater 1997;35(4):574–84.
[47] Sainz-Garcia A, et al. Assessment of feasible strategies for seasonal underground hydrogen storage in a saline aquifer. Int J Hydrogen Energy 2017;42(26):16657–66.
[48] Harati S, et al. Underground hydrogen storage to balance seasonal variations in energy demand: impact of well configuration on storage performance in deep saline aquifers. Int J Hydrogen Energy 2023;48(69):26894–910.
[49] Jia C, et al. Numerical studies of hydrogen buoyant flow in storage aquifers. Fuel 2023;349:128755.

[50] Peng DY, Robinson DB. A new two-constant equation of state. Ind Eng Chem Fundam 1976;15(1):59–64.
[51] Stiel LI, Thodos G. The viscosity of nonpolar gases at normal pressures. AIChE J 1961;7(4):611–5.
[52] Chabab S, et al. Measurements and predictive models of high-pressure H_2 solubility in brine (H_2O+NaCl) for underground hydrogen storage application. Int J Hydrogen Energy 2020;45(56):32206–20.
[53] Kim SB. Numerical analysis of bacterial transport in saturated porous media. Hydrol Process: Int J 2006;20(5):1177–86.
[54] Zhao Q, et al. Numerical simulation of the impact of different cushion gases on underground hydrogen storage in aquifers based on an experimentally-benchmarked equation-of-state. Int J Hydrogen Energy 2024;50:495–511.